


ARTICLE

<https://doi.org/10.1038/s41467-019-13237-8>

OPEN

Glycogen branching enzyme controls cellular iron homeostasis via Iron Regulatory Protein 1 and mitoNEET

Nhan Huynh¹, Qiuxiang Ou¹, Pendleton Cox¹, Roland Lill ^{2,3} & Kirst King-Jones ^{1*}

Iron Regulatory Protein 1 (IRP1) is a bifunctional cytosolic iron sensor. When iron levels are normal, IRP1 harbours an iron-sulphur cluster (holo-IRP1), an enzyme with aconitase activity. When iron levels fall, IRP1 loses the cluster (apo-IRP1) and binds to iron-responsive elements (IREs) in messenger RNAs (mRNAs) encoding proteins involved in cellular iron uptake, distribution, and storage. Here we show that mutations in the *Drosophila* 1,4-Alpha-Glucan Branching Enzyme (*AGBE*) gene cause porphyria. *AGBE* was hitherto only linked to glycogen metabolism and a fatal human disorder known as glycogen storage disease type IV. *AGBE* binds specifically to holo-IRP1 and to mitoNEET, a protein capable of repairing IRP1 iron-sulphur clusters. This interaction ensures nuclear translocation of holo-IRP1 and down-regulation of iron-dependent processes, demonstrating that holo-IRP1 functions not just as an aconitase, but throttles target gene expression in anticipation of declining iron requirements.

¹Department of Biological Sciences, University of Alberta, G-504 Biological Sciences Bldg, Edmonton, Alberta T6G 2E9, Canada. ²Institut für Zytobiologie und Zytopathologie, Philipps-Universität Marburg, Robert-Koch-Strasse 6, 35032 Marburg, Germany. ³LOEWE Zentrum für Synthetische Mikrobiologie SynMikro, Philipps-Universität Marburg, Hans-Meerwein-Straße, 35043 Marburg, Germany. *email: kirst.king-jones@ualberta.ca

Iron is an essential trace element for nearly all organisms and cells, because iron co-factors, most commonly in the form of haem and iron–sulfur (Fe–S) clusters^{1,2}, are required for a wide range of protein functions. While essential, free iron is also highly reactive and cytotoxic, and thus its acquisition requires tight regulation by cells². IRP1 is a bifunctional protein because it can reversibly bind to Fe–S clusters³. Under iron-replete conditions, the protein forms holo-IRP1 and acts as a cytosolic aconitase, an enzyme that interconverts citrate and isocitrate. When cellular iron levels drop, IRP1 loses its Fe–S cluster and assumes a different conformation⁴, apo-IRP1, which then binds to and regulates specific target mRNAs containing iron-responsive elements (IREs). This action can either block translation or enhance transcript stability, depending on the location of the IRE, with a net outcome that promotes increased cellular iron availability and trafficking⁵.

Current models for studying cellular iron homeostasis are limited in the sense that they have either static, or at best, linearly increasing iron requirements (cell cultures and developing erythrocytes, respectively)^{2,6}. We introduce here the *Drosophila* prothoracic gland (PG) as a model to study highly dynamic iron requirements. The PG is an endocrine tissue mainly devoted to the production of steroid hormones in developing insects. In both vertebrates and insects, the synthesis of steroid hormones is largely dependent on enzymes that require haem and Fe–S clusters^{7,8}. In *Drosophila*, the PG is the principal steroid-producing gland, and part of a larger endocrine tissue called the ring gland. During larval development, the PG produces pulses of the steroid hormone ecdysone (E), which acts as a recurring systemic signal that controls gene expression in target tissues to coordinate hatching, moulting, and metamorphosis (Supplementary Fig. 1). The first step of E biosynthesis is carried out by Neverland, which harbours an Fe–S cluster⁹, while all but one of the following reactions are carried out by cytochrome P450 proteins, which require haem as an obligate co-factor (Fig. 1a). The last larval stage of *Drosophila* development is accompanied by exceedingly high expression of ecdysone-producing enzyme (“Halloween”) genes (Supplementary Fig. 1)⁸, indicating that the PG requires substantial amounts of iron, which can be visualized by staining for ferric iron (Fig. 1b). PG cells have fluctuating iron and haem demands because they must match the rise and fall of Halloween enzyme levels with appropriate production rates of iron co-factors. Thus, the PG represents a powerful model to study mechanisms by which cells control dynamic changes in cellular iron and haem requirements. We show here that the *Drosophila* Glycogen Branching Enzyme (AGBE) is a regulator of iron homeostasis. AGBE interacts physically with the holoform of Iron Regulatory Protein 1A (IRP1A) and Cisd2, an ortholog of vertebrate mitoNEET. This synergistic interaction ensures that holo-IRP1A remains functional. Further, we show that holo-IRP1A has a surprising new role in the nucleus, where it transcriptionally downregulates genes acting in steroid hormone biosynthesis as well as iron and heme metabolism.

Results

Loss of glycogen branching enzyme causes porphyria-like phenotypes. The haem biosynthetic pathway is highly conserved in metazoans and fungi and comprises eight enzymatic steps that convert glycine and Succinyl-CoA to mature haem (Fig. 1c)¹⁰. Exposure to air and UV light isomerizes porphyrinogen rings, first produced in step 4, into autofluorescing porphyrins, but incorporation of iron into protoporphyrin IX results in non-fluorescing haem (Fig. 1d)^{10,11}. We noticed the presence of red autofluorescence in the PG when we exposed larvae from four RNAi lines to UV light (targeting *Updo*, *Ppox*, *spz5*, and *AGBE*),

all of which had been identified in two unrelated PG-specific RNA interference (RNAi) screens^{7,8}. Also, the ring glands were enlarged compared to time-matched controls and had a red-brown appearance under brightfield light (Supplementary Fig. 2). A fifth RNAi line, *Nos^{IR-X}*, targeting the *nitric oxide synthase* (*Nos*) gene, had been reported to produce large red-brown PGs¹², and when re-examined by us, also showed red autofluorescence (Fig. 1e). Consistent with their role in haem biosynthesis, depleting *Updo* (=vertebrate UROD, Supplementary Fig. 3) and *Ppox* caused protoporphyrin accumulation in the PG. This is equivalent to what occurs in patients afflicted with porphyria, a group of rare diseases impairing haem biosynthesis¹³. PG-specific *Alas*-RNAi, on the other hand, disrupts haem synthesis prior to porphyrinogen ring formation, and therefore lacked the autofluorescence, but causes enlarged ring glands (Fig. 1e). We then sought to validate the three remaining lines, *Nos^{IR-X}*, *AGBE^{IR1}*, and *spz5^{IR}*, since their relationship to haem biosynthesis was intriguing. We were unsuccessful in finding independent evidence for the *Nos^{IR-X}* and *spz5^{IR}* lines, suggesting that the phenotypes were caused by off-target effects. However, a second, non-overlapping RNAi line targeting *AGBE*, *AGBE^{IR2}*, caused similar phenotypes (Fig. 1f). *AGBE* encodes a glycogen branching enzyme, which is an essential enzyme that acts in glycogen biosynthesis¹⁴. There are, however, no reports that link glycogen branching enzymes to iron or haem homeostasis. Therefore, we further validated these results by using CRISPR/CAS9 to replace the endogenous *AGBE* gene with a genomic copy that was flanked by Flippase (FLP) Recombinase Target (FRT) sites, and where the last exon extended into a Flag- or Myc-tag (*AGBE^{FCF}* and *AGBE^{FCM}*, Supplementary Fig. 4). Excision of the conditional *AGBE^{FCF}* allele via PG-specific expression of FLP confirmed the *AGBE*-RNAi phenotypes, as we observed strong autofluorescence with overall higher penetrance than the two RNAi lines, since no adults eclosed compared to 4.6% in homozygous *PG > AGBE^{IR1}* animals (Fig. 1f, g).

We reasoned that a lack of cellular or mitochondrial iron could disrupt haem production and may explain the porphyria phenotype in *AGBE*-loss-of-function lines. Remarkably, upon rearing *PG > AGBE^{IR1}* and *PG > FLP; AGBE^{FCF}* larvae on an iron-supplemented diet, the autofluorescence was absent (Fig. 1f), and we observed that ~40–50% of the larvae now developed into phenotypically normal adults (Fig. 1g). In agreement with this, adding the iron chelator bathophenanthroline sulfate (BPS) slightly decreased survival rates, while adding both iron and BPS to the diet reversed the rescue seen by iron alone, confirming that BPS is an effective tool to reduce available iron. *AGBE*-RNAi larvae were uniquely rescued by dietary iron, since neither *Alas*-, *Updo*-, *Ppox*-, *Nos*- or *spz5*-RNAi lines benefited from iron supplementation (not shown). *AGBE* expression was moderately upregulated under iron-chelating conditions, consistent with the idea that the gene partakes in cellular iron homeostasis (Fig. 1h). Next, we tested whether disrupting four other glycogen biosynthesis genes via PG-specific RNAi would phenocopy *AGBE*-depletion (Supplementary Fig. 5). This neither caused autofluorescence nor significant lethality. However, ubiquitous expression of RNAi targeting these glycogen biosynthesis genes caused widespread larval lethality, confirming that all RNAi transgenes in these lines were expressed, which suggested that the disruption of glycogen biosynthesis per se in the PG did not cause any iron- or haem-related phenotypes, but was a unique feature of *AGBE*.

Glycogen branching enzyme physically interacts with Iron Regulatory Protein 1 (IRP1). *AGBE* is the single orthologue of vertebrate GBE1 (Glycogen Branching Enzyme 1), and the two

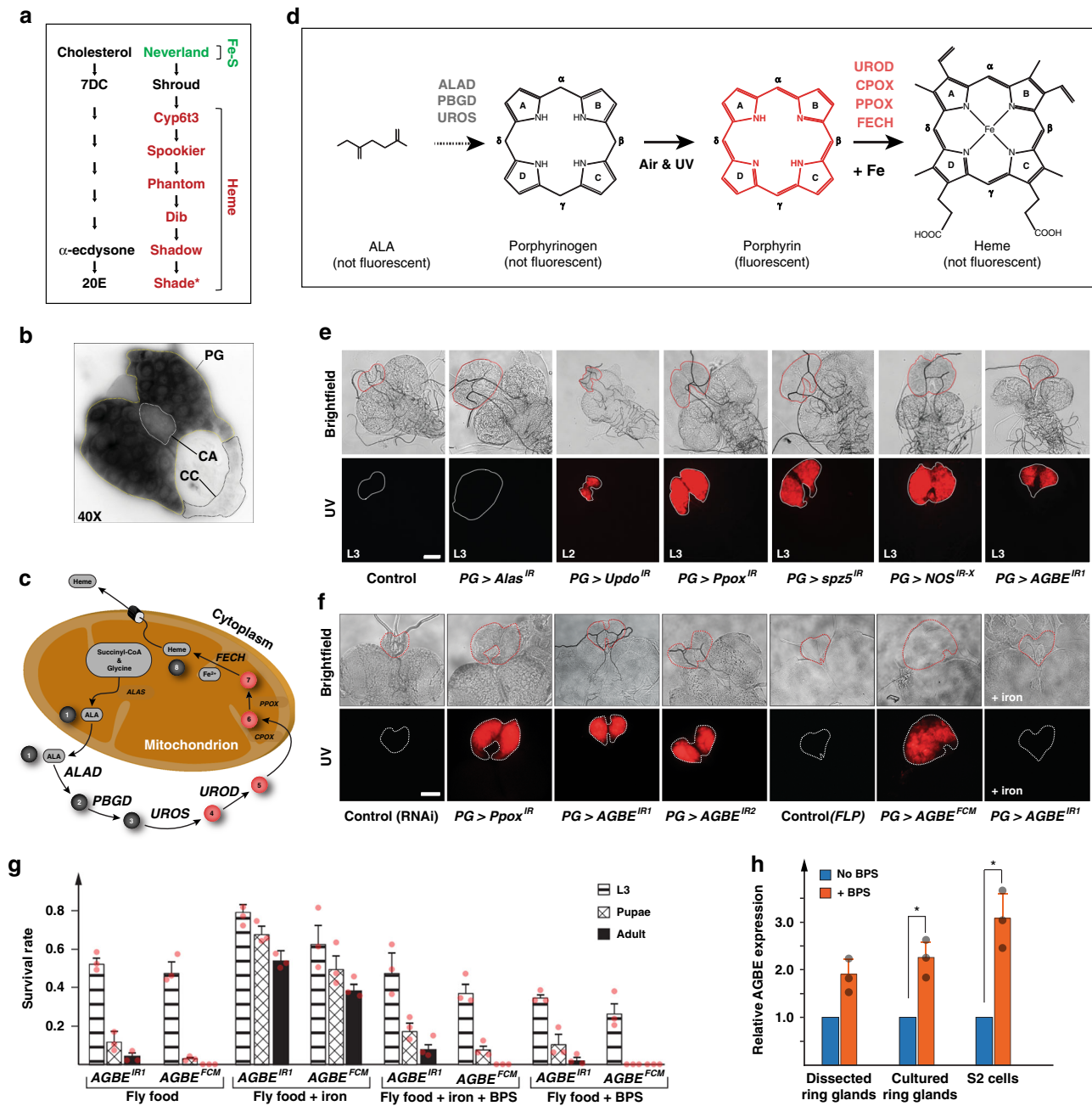


Fig. 1 Disruption of haem biosynthesis in the *Drosophila* prothoracic gland (PG). **a** Ecdysone biosynthetic pathway converts cholesterol to α -ecdysone, which is metabolized to 20OH-ecdysone in target cells by Shade (*not or lowly expressed in the PG). All enzymes except for Shroud require iron co-factors in the form of iron-sulfur (Fe-S) clusters or haem. **b** Stain for ferric (non-haem-bound) iron in the ring gland. The corpus allatum (CA) and the corpora cardiaca (CC) are neighbouring glands fused to the PG. **c** Haem biosynthesis pathway in metazoans and yeast. Red circles represent protoporphyrin intermediates that autofluoresce. **d** Autofluorescence of porphyrins occurs through isomerization of porphyrinogens exposed to air and UV light. **e** UV exposure of dissected ring glands from RNAi lines (designated as gene^{IR}) from second (L2) or third (L3) instar stages. *Alas*, *Updo*, and *Ppox* encode haem-synthesizing enzymes. *spz5*: spaetzle5, *Nos*: nitric oxide synthase, *AGBE*: 1,4-Alpha-Glucan Branching Enzyme. Scale bar = 250 μ m. **f** UV exposure of dissected ring glands isolated at 40 h after the L2/L3 moult (~8 h prior to pupariation in controls). RNAi lines *AGBE*^{IR1} and *AGBE*^{IR2} target distinct regions of the *AGBE* mRNA. *AGBE*^{FCM} is a conditional CRISPR-knock-in allele that can be excised in a tissue-specific manner via the expression of Flippase (FLP) recombinase (Supplementary Fig. 4). + iron: larvae were reared on a diet containing ferric ammonium citrate (FAC) as an iron supplement. Scale bar = 250 μ m. **g** Survival of *AGBE*^{IR1} and *AGBE*^{FCM} larvae fly food supplemented with iron (FAC) or an iron chelator, bathophenanthroline sulfate (BPS). Error bars represent standard deviation. Three biological replicates, with each sample containing 50 individuals. **h** Relative *AGBE* mRNA expression levels. Dissected ring glands: isolated from L3 reared on media \pm BPS. Cultured ring glands: isolated from L3 reared on normal media, but then transferred to buffer containing \pm BPS. S2 cells: Schneider 2 cells grown on medium \pm BPS. mRNA levels were analysed via quantitative real-time PCR. For primers see Table 3. Asterisk indicates a *P*-value < 0.05 based on the Student's *t* test. Error bars represent 95% confidence intervals. Each of the three biological replicates was tested three times. Source data are provided as a Source Data file.

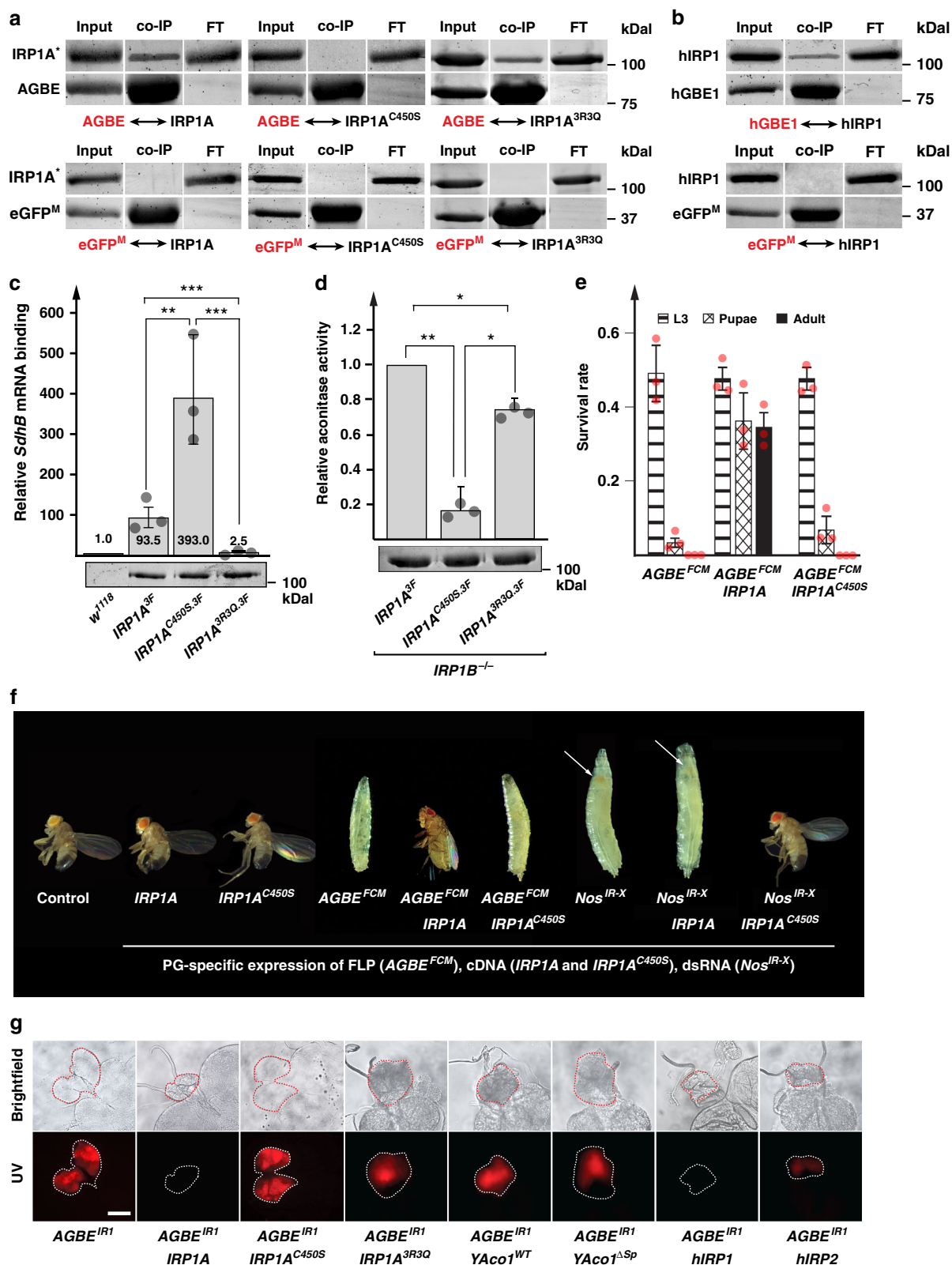
proteins are 61% identical. A search of protein–protein interaction databases^{15,16} revealed that human GBE1 physically interacts with IRP1. Vertebrates have two *IRP* genes, IRP1 and IRP2, but only IRP1 can switch between the aconitase and the RNA-binding form, while IRP2 lacks the Fe–S cluster and is constitutively RNA-binding³. *Drosophila* does not have the *IRP2* gene but harbours two *IRP1* genes (*IRP1A* and *IRP1B*) (Supplementary Fig. 6). Only *IRP1A* has been shown to switch from holo- to the IRE-binding apoform, while *IRP1B* is believed to act only as an aconitase, as it failed to bind canonical IREs¹⁷. The reported interaction between GBE1 and IRP1 raised the possibility that *Drosophila* AGBE and human GBE1 function in the regulation of iron homeostasis by modulating IRP1 activity. Using a cell culture approach, we established that the interaction also occurred in *Drosophila*, namely between AGBE and *IRP1A* (Fig. 2a), and we recapitulated the interaction between human IRP1 and GBE1 in the same system (Fig. 2b). AGBE interacted robustly with wild type *IRP1A*, as well as with *IRP1A*^{3R3Q}, which carries three point mutations (R549Q, R554Q, R793Q, see Supplementary Fig. 4) predicted to disrupt RNA-binding¹⁸. Strikingly, a single point mutation that prevents Fe–S cluster binding to *IRP1A* (predicted to generate constitutively RNA-binding *IRP1A*^{C450S}) abolished the interaction with AGBE (Fig. 2a), suggesting that holo-*IRP1A* is the in vivo binding partner of AGBE. This was paradoxical, as AGBE mutations caused iron-deficiency phenotypes, but holo-*IRP1A* has no known roles in iron homeostasis as it is believed to only act as an aconitase. To examine whether the *IRP1A*^{3R3Q} and *IRP1A*^{C450S} forms acted as predicted, we tested their in vivo ability to bind an IRE-containing mRNA (*SdhB*) and whether either of them had aconitase activity (Fig. 2c, d). As expected, the *IRP1A*^{3R3Q} form displayed strongly reduced mRNA-binding compared to both the wild type and the *IRP1A*^{C450S} forms (Fig. 2c). Likewise, both knocked-in and transgenic alleles of *IRP1A*^{C450S} resulted in significantly reduced aconitase activity compared to wild type *IRP1A* and the *IRP1A*^{3R3Q} form (Fig. 2d and Supplementary Fig. 7).

To further substantiate the interaction between AGBE and holo-*IRP1A*, we carried out a series of MALDI-TOF-based mass spectrometry (MS) experiments (see later section). We also sought to validate this interaction by genetic means. For the latter, we tested whether animals with PG-specific loss of AGBE function could be rescued by expressing transgenic wild type *IRP1A* or *IRP1A*^{C450S} (Supplementary Table 1). Remarkably, wild type *IRP1A* rescued both the larval lethality (Fig. 2e, f) as well as the porphyria phenotype of animals that lacked functional AGBE (Fig. 2g), while *IRP1A*^{C450S} was completely ineffective (Fig. 2e, g). It was possible that the *IRP1A*^{C450S} allele was not functional, despite differing only in a single point mutation from *IRP1A*. However, when we expressed *IRP1A*^{C450S} in other genetic backgrounds, we observed dramatic rescue of *PG > NOS^{IR-X}* RNAi animals with respect to both the lethality (Fig. 2f) and protoporphyrin accumulation (not shown). Also, our immunoprecipitation results showed that *IRP1A*^{C450S} is RNA-binding (Fig. 2c). Taken together, these data demonstrated that *IRP1A*^{C450S} was fully active but not sufficient to compensate for the iron deficiency in AGBE-depleted animals, suggesting that holo-*IRP1A* has functions beyond the aconitase that are important for iron homeostasis. To test whether the aconitase function of holo-*IRP1A* had unexpected essential functions, we attempted rescuing *AGBE^{FCM}* mutants with the aconitase-only form of *IRP1A* (*IRP1A*^{3R3Q}), as well as a cytosolic and mitochondrial version of yeast aconitase (*YAcO1^{WT}* and *YAcO1^{ΔSp}*, respectively), neither of which can switch to the RNA-binding form^{18,19}. None of these approaches rescued the loss-of-AGBE-function phenotypes (Fig. 2g), indicating that both holo- and apo-*IRP1A* were required for survival. Lastly, we

crossed human *IRP1* (*hIRP1*) and *IRP2* (*hIRP2*) into the *AGBE^{IR1}*-RNAi strain. Consistent with the above findings, only *hIRP1* (equivalent to *IRP1A*, Supplementary Fig. 6) could fully rescue *AGBE^{IR1}* larvae, while constitutively RNA-binding *hIRP2*, was much less effective (Fig. 2g), albeit more efficient than *IRP1A*^{C450S}, suggesting partial rescue by *hIRP2*.

Since no null mutations were available for *IRP1A* or *IRP1B*, we needed to establish that a) these genes had indeed roles in *Drosophila* iron regulation and if so, b) whether *IRP1A* and *IRP1B* had distinct roles in controlling cellular iron levels, c) whether these genes were required in the PG, and d) whether this would phenocopy AGBE-depletion in the PG. We first disrupted both *IRP1A* and *IRP1B* in the PG via RNAi (*PG > IRP1A^{IR}* and *PG > IRP1B^{IR}*). On regular fly food, neither RNAi line resulted in obvious phenotypes. However, when flies were reared on iron-depleted fly food for three generations, *PG > IRP1A^{IR}* animals displayed significant larval lethality, with a concomitant appearance of red autofluorescence in the larval PG (Fig. 3a). Control and *PG > IRP1B^{IR}* populations did not exhibit lethality until the 5th generation, and larvae never showed any autofluorescence (not shown and Supplementary Fig. 8). To confirm these data, we used two approaches. First, we generated a Flag-tagged and FRT-flanked knock-in allele of endogenous *IRP1A* (*IRP1A^{FCF}*), allowing us to excise the gene via PG-specific expression of *FLP* (Supplementary Fig. 4). This approach resulted in red-fluorescing PGs in *PG > FLP;IRP1A^{FCF}* larvae that were switched from iron-replete to BPS-containing media (Fig. 3b). However, homozygous *IRP1A^{FCF}* flies were not viable on regular fly media, indicating that the inserted *FRT* sites had generated a loss-of-*IRP1A*-function allele. Therefore, we employed a second CRISPR strategy, where we crossed flies that specifically expressed *CAS9* in the PG²⁰ to flies expressing two gRNAs that targeted *IRP1A* (Supplementary Table 1). The resulting F1 progeny also displayed PG-specific autofluorescence and 100% lethality on regular fly media (Fig. 3b). To complement these PG-specific lesions with classic mutant analysis, we examined an existing mutant *IRP1A* line (Bloomington #30181). However, we did not consider this allele further as it turned out to be a weak hypomorph. We, therefore, generated deletion mutants for *IRP1A* and *IRP1B* using CRISPR/CAS9, designated here as *IRP1A^{KO}* and *IRP1B^{KO}*. On regular fly food, *IRP1A^{KO}* mutants died as first (L1) and second instar larvae (L2), but were able to develop into phenotypically normal adults when reared on an iron-supplemented diet (Fig. 3c), indicating that *IRP1A* was essential for responding to iron-poor conditions. In contrast, *IRP1B* mutants revealed no obvious phenotypes under any of the tested conditions. Taken together, these results showed that *IRP1A* is the principal regulator of cellular iron homeostasis in *Drosophila* and that *IRP1A* depletion phenocopied the iron-dependent porphyria seen in AGBE mutants.

Subcellular localization of apo- and holo-IRP1. We then addressed whether holo-*IRP1A* had unanticipated roles in the regulation of cellular iron homeostasis, since only the holoform interacted with AGBE, and was required to rescue AGBE mutants. When we carried out immunolocalisation of *PG > 3xFlag-IRP1A^{WT}* and *PG > 3xFlag-IRP1B^{WT}* transgenic lines (Supplementary Table 1), we found that both *IRP1A* and *IRP1B* were enriched in PG nuclei (Fig. 3d). In stark contrast, expressing the single-point mutation variants *IRP1A*^{C450S} or *IRP1B*^{C447S} (which abolishes Fe–S-binding in *IRP1B*, Supplementary Table 1) resulted in predominantly cytoplasmic accumulation of either protein (Fig. 3d). Similarly, we found that human *IRP1* localises to PG nuclei as well, while human *IRP2* failed to do so (Fig. 3e). This behaviour is consistent with the absence of an Fe–S cluster in



hIRP2, indicating that nuclear accumulation strongly favours holo-IRP proteins.

Given the interaction between AGBE and holo-IRP1A, we wondered whether entry of IRP1A into nuclei was dependent on AGBE. For this, we crossed the Flag-tagged IRP1A^{3F} and IRP1B^{3F} knock-in alleles (Supplementary Fig. 4) into AGBE mutants. This approach revealed that IRP1A, but not IRP1B, was dependent on

AGBE for nuclear translocation (Fig. 3f), suggesting that IRP1A requires AGBE for maintaining Fe-S clusters, which in turn are needed for nuclear entry. Finally, we determined the subcellular localisation of IRP1A^{3F} and IRP1B^{3F} in other tissues. Both IRP1A and IRP1B showed strong cytoplasmic and negligible nuclear presence in the larval salivary gland, while the adjacent fat body displayed predominantly nuclear IRP1A and IRP1B (Fig. 3g).

Fig. 2 AGBE interacts with IRP1A. **a** Co-transfection of S2 cells with plasmids encoding Flag-tagged IRP1A variants (IRP1A^Δ) and Myc-tagged AGBE followed by immunoprecipitation via anti-Myc antibodies and Western blotting. Names shown in red indicate the protein used as bait. IRP1A: wild type IRP1A, IRP1A^{C450S}: constitutively RNA-binding IRP1A, IRP1A^{3R3Q}: non-RNA-binding form of IRP1A (Supplementary Table 1). Myc-tagged enhanced GFP (eGFP^M) served as a negative control. Input lane represents 10% of the sample. Presence of co-immunoprecipitated proteins were tested with anti-Flag antibodies. **b** Like A, but co-transfection of S2 cells with plasmids encoding Flag-tagged human IRP1 (aka Aco1) and Myc-tagged human GBE1, as well as eGFP^M as a negative control. **c** Quantitative RNA-immunoprecipitation (RIP). Samples from larvae carrying Flag-tagged knock-in alleles of *IRP1A* (*IRP1A*^{3F}, *IRP1A*^{C450S.3F}, and *IRP1A*^{3R3Q.3F}) (Supplementary Fig. 4) were normalized via Western blotting to visualize Flag-tagged proteins followed by ImageJ quantification. Western blot of adjusted samples shown below graph. Untagged IRP1A (control line *w¹¹¹⁸*) served as a negative control and calibrator (normalized expression = 1). *SdhB* mRNA harbours a validated IRE^{72,73}. Co-immunoprecipitated *SdhB* mRNA was quantified via qPCR. Error bars represent 95% confidence intervals from three biological replicates. ****p* < 0.001, ***p* < 0.01, **p* < 0.05. **d** Aconitase activity. Same *IRP1A* alleles and normalization procedure as described in **c**, except that *IRP1A*^{3F} served as the control (normalized to 1). All alleles were crossed into an *IRP1B*^{-/-} mutant background to eliminate the aconitase activity of IRP1B. Further, we removed mitochondria via ultracentrifugation to reduce the contribution of mitochondrial aconitase. Error bars represent standard deviation from three biological replicates. ***p* < 0.01, **p* < 0.05. **e** Survival rates of *PG > FLP; AGBE^{FCM}* animals (Supplementary Fig. 4), which causes Flippase-mediated excision of the AGBE transcription unit specifically in the prothoracic gland (PG). Tested in either the presence or absence of the *IRP1A* and *IRP1A*^{C450S} transgenes that are also expressed in a PG-specific manner. Error bars represent standard deviation from three biological replicates (each sample contained 50 individuals). **f** Larval and adult phenotypes of *PG > FLP; AGBE^{FCM}* and *PG > Nos^{IR-X}* animals expressing *IRP1A*^{C450S} or wild type *IRP1A* transgenes. Arrows point to red-stained PG. **g** Ring glands dissected from *PG > AGBE^{IR1}* larvae in the presence or absence of the following transgenic cDNAs: *IRP1A* (wild type *IRP1A*); *IRP1A*^{C450S} (constitutively RNA-binding); *IRP1A*^{3R3Q} (non-RNA-binding); *Yaco1^{WT}*: wild type yeast aconitase (mitochondrial); *Yaco1^{ΔSp}* (cytoplasmic); *hIRP1* & *hIRP2*: human IRP1 & IRP2. Scale bar = 250 μm. All transgenes are expressed in a PG-specific manner via the Gal4-UAS system. Source data are provided as a Source Data file.

This strongly suggests that nuclear translocation of IRP1 proteins is highly tissue-specific, and not a function of systemic iron load, and hence may reflect tissue-specific iron requirements. Given that human IRP1 also localises to *Drosophila* nuclei, this raises the question of whether vertebrate IRP1 may also enter nuclei in specific tissues or during specific developmental/physiological conditions.

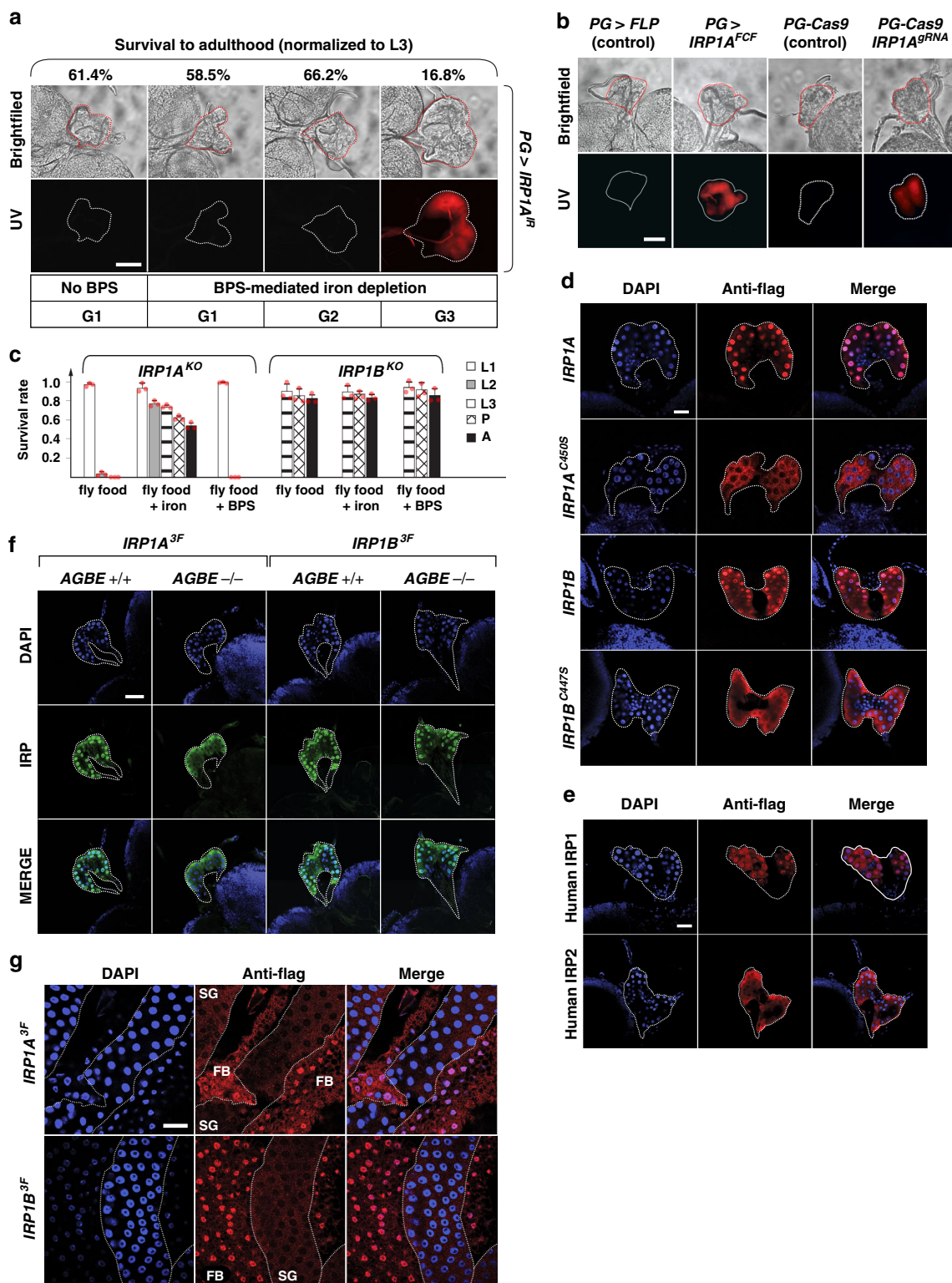
We next sought to identify proteins that would physically interact with IRP1A and IRP1B in order to shed light on the interaction with AGBE and the presence of both IRP1s in nuclei. For this, we immunoprecipitated endogenous or transgenic versions of Flag-tagged AGBE, IRP1A and IRP1B and subjected ring gland and whole-body samples to MS, for a total of 17 conditions (Supplementary Table 2). As controls, we used a total of five wild type samples (which lack Flag-tagged proteins), processed them in parallel to the experimental samples, and removed all proteins found in the controls from the experimental data sets (Supplementary Data 1). Briefly, the interactome for IRP1A indicated extensive interactions with ribosomal proteins and eukaryotic initiation factors, consistent with previous findings^{21,22} and IRP's role in regulating translation. We also identified four histone proteins for IRP1A (H4, H2A, H2B, and H2Av) and two for IRP1B (H4 and H2A), consistent with the presence of both IRP1s in nuclei (Fig. 4a and Supplementary Data 1–2). Importantly, endogenously tagged AGBE^{FCF} specifically pulled down a total of 22 proteins from whole-body samples (Fig. 4b), which included IRP1A, IRP1B and Cisd2, an Fe-S protein. Vertebrate Cisd1, Cisd2, and Cisd3 comprise a small family referred to as the NEET proteins²³, which harbour an unusual 2Fe-2S cluster that enables these proteins to transfer their cluster to other proteins^{24–26}. *Drosophila* encodes only two NEET proteins, Cisd2 and CG3420 (=> Cisd3), where Cisd2 lies evolutionary between human mitoNEET (encoded by Cisd1) and Naf-1 (encoded by Cisd2)²⁷, and as such, fly Cisd2 may be functionally related to both.

We also used endogenously tagged IRP1A (IRP1A^{3F}) as bait, which co-immunoprecipitated 166 proteins that included AGBE, Cisd2, and IRP1B, as well as two ferritins (iron storage proteins), Fer1HCH and Fer2LCH (Fig. 4a, b and Supplementary Data 1–2). Both AGBE and IRP1A interacted with another glycogen enzyme, glycogen synthase (GlyS), further corroborating that cellular iron homeostasis and glycogen metabolism are physically linked. IRP1B pulled down AGBE and the histones H2A and H4, but not

Cisd2. For IRP1A, all above interactions, with the exception of GlyS, were validated by PG-specific MS (Fig. 4a and Supplementary Data 1). Finally, we further validated these MS data with samples from four fly strains that expressed one of the following transgenes: apo-IRP1A (*IRP1A*^{C450S}); apo-IRP1B (*IRP1B*^{C447S}); non-RNA-binding IRP1A (*IRP1A*^{3R3Q}) and IRP1B (*IRP1B*^{3R3Q}) (Supplementary Tables 1–2). This approach confirmed the results seen with the knock-in alleles, and, importantly, showed that IRP1A^{C450S} failed to interact with AGBE, while Cisd2 interacted with both IRP1A variants, but none of the IRP1B proteins (Supplementary Fig. 9).

Since iron-depletion triggers the switch from holo- to apo-IRP1A, one would predict that this results in cytoplasmic accumulation of IRP1A and should, therefore, alter the interactome of this protein. When we reared flies for three generations on BPS-containing media, we noticed that it takes two generations to purge IRP1A and IRP1B from PG nuclei (Supplementary Fig. 10). In the fat body, however, it takes only one generation for IRP1A to become entirely cytoplasmic, while IRP1B is still nuclear after three generations of iron-depletion (Supplementary Fig. 11), suggesting that IRPs have tissue-specific behaviours. To test whether iron-depletion affected protein-protein interactions of IRP1A, we reared endogenously tagged IRP1A^{3F} flies for two generations on BPS-supplemented food and conducted MS from whole-body larval samples. This strategy reduced the number of co-immunoprecipitated proteins from 166 (no BPS) to 117 (in G1 = one generation BPS) and 30 (in G2 = two generations of BPS) (Supplementary Data 1). Consistent with the cytoplasmic localisation of IRP1A on BPS media, the interaction with histone H2Av and H2B was lost in G1, and none of the four histone proteins were detected in G2, which resembles the pattern seen in the co-immunoprecipitation results with the cytoplasmic IRP1A^{C450S} protein (Supplementary Data 1). Further, binding to AGBE was lost in G1 and G2, consistent with our finding that AGBE only interacts with holo-IRP1A. The interaction between IRP1A and IRP1B was lost in G2, while binding to Fer2LCH was detectable in all conditions. The top-scoring protein in G2 was Cisd2/mitoNEET (Supplementary Data 1), indicating that the IRP1A-Cisd2/mitoNEET interaction was robust even when iron levels were low.

MitoNEET mutants phenocopy IRP1A and AGBE mutants. MitoNEET is a homodimeric Fe-S protein that resides in the



outer mitochondrial membrane, with the Fe-S cluster facing the cytosol²³. While the exact range of functions for mitoNEET remains unclear, the protein has been shown to act in the repair of oxidatively damaged vertebrate IRP1 Fe-S clusters^{23,28}. Since the MS data suggested that Cisd2/mitoNEET represents an important link between AGBE and IRP1A, we sought validation by molecular and genetic means. First, we validated the physical interaction via co-immunoprecipitation assays in *Drosophila*

Schneider 2 cells (S2) cells. This showed that both AGBE and IRP1A physically interact with Cisd2 (Fig. 4c). However, this interaction was ~3-fold enhanced when AGBE and IRP1A were co-transfected together with Cisd2 (Fig. 4c, d), suggesting synergistic interactions between the three proteins.

Next, we examined Cisd2 function by genetic means. When we depleted Cisd2 via RNAi in the PG or examined a *Cisd2* mutant, flies survived on regular food, and displayed no protoporphyrin

Fig. 3 IRP1 localizes to nuclei. **a** Protoporphyrin accumulation/autofluorescence in prothoracic glands (PG) from *IRP1A*-RNAi (*IRP1A^{IR}*) flies reared on iron-depleted (=BPS) media for three generations. Adult survival relative to last larval stage (surviving third instar larvae = L3 = 100%). Scale bar = 250 μ m. **b** Protoporphyrin accumulation/autofluorescence in PGs from *IRP1A^{FCF}* animals (tissue-specific excision of *IRP1A*, Supplementary Fig. 4) reared on iron-rich medium until L2, after which larvae were switched to BPS-supplemented food. Scale bar = 250 μ m. **c** Survival of *IRP1A* and *IRP1B* null mutants (KO = knockout, Supplementary Fig. 4). Error bars represent standard deviation from three biological replicates (each sample contained 50 individuals). **d** Subcellular localization of PG-specific, Flag-tagged IRP1A and IRP1B (*PG > IRP1A/PG > IRP1B* transgenic lines, Supplementary Table 1). DAPI was used to stain DNA/nuclei. Scale bar = 250 μ m. **e** Subcellular localization of Flag-tagged transgenic human IRP1 and IRP2 (*PG > hIRP1* and *PG > hIRP2*, Supplementary Table 1) expressed specifically in the PG. Scale bar = 250 μ m. **f** Subcellular localization of Flag-tagged proteins encoded by *IRP1A^{3F}* and *IRP1B^{3F}* knock-in alleles (Supplementary Fig. 4) in control or *AGBE* mutant backgrounds (*AGBE^{+/+}* = *PG > FLP*; *AGBE^{-/-}* = *PG > FLP*; *AGBE^{FCM}*, Supplementary Fig. 4). Scale bar = 500 μ m. **g** Subcellular localization of Flag-tagged proteins encoded by *IRP1A^{3F}* and *IRP1B^{3F}* knock-in alleles (Supplementary Fig. 4) in the fat body (FB) and salivary gland (SG). Scale bar = 500 μ m. Source data are provided as a Source Data file.

accumulation (Fig. 4e, f). On BPS media, however, most (*Cisd2* mutant) or all (*Cisd2*-RNAi) animals arrested development during the third instar and displayed red autofluorescence in the PG (Fig. 4e, f). We then tested whether *Cisd2* and IRP1A interacted genetically, and therefore analysed RNAi lines targeting *Drosophila Cisd2*, *IRP1A* and *IRP1B* alone and in combination. None of the individual PG > RNAi larvae displayed any overt phenotypes when reared on regular fly media. However, when we combined *IRP1A*- with *Cisd2*-RNAi, we observed strong synthetic lethality, where none of the larvae reached adulthood, and importantly, all larvae displayed protoporphyrin accumulation in the PG (Fig. 4g), indicating that both proteins participate in the same process. In contrast, the combination of *IRP1B*- with *Cisd2*-RNAi was as ineffective as the individual lines alone. We concluded that the functional importance of the IRP1-mitoNEET interaction is conserved between vertebrates and *Drosophila* and that this process is essential, at least in *Drosophila*. Finally, we tested whether IRP1A and IRP1B could localise to nuclei in a *Cisd2*-mutant background. To test this, we crossed flies that harboured Flag-tagged *IRP1A^{3F}* or *IRP1B^{3F}* knock-in alleles into a *Cisd2*-mutant background and reared them on fly food in the presence or absence of BPS. On regular fly food, both proteins were nuclear, while exposure to BPS shifted their subcellular distribution to the cytoplasm of the PG (Fig. 4h). Control flies reared for one generation on BPS-containing food still show predominantly nuclear IRP1A and IRP1B in the PG (Supplementary Fig. 10). Taken together, these data indicate that *AGBE*, *Cisd2*/mitoNEET, and IRP1A act together to ensure that holo-IRP1A remains functional and can enter the nucleus.

Nuclear IRP1. An intriguing possibility is that holo-IRP1 has additional roles in the nucleus that contribute to tissue-specific cellular iron homeostasis. This is supported by the MS data, which indicates distinct but overlapping binding behaviours by IRP1A and IRP1B to histone proteins. To examine this further, we carried out genome-wide transcript profiling of hand-dissected ring glands (which contain the PG) that expressed one of six Flag-tagged transgenes in a PG-specific manner: *IRP1A^{WT}* and *IRP1B^{WT}*, which are both wild type; *IRP1A^{C450S}* and *IRP1B^{C447S}*, both of which can only assume the apo-form and are predominantly cytoplasmic; as well as *IRP1A^{3R3Q}* and *IRP1B^{3R3Q}*, both of which are presumed to be non-RNA-binding and can enter nuclei (not shown) (Supplementary Table 1). The design of this approach was based on the idea that the transcriptional changes elicited by *IRP1A^{3R3Q}* and *IRP1B^{3R3Q}* should largely result from their nuclear function, as they are predicted to have lost RNA-binding capability. When we examined the 234 most significantly downregulated genes by *IRP1A^{3R3Q}*, we noticed strong enrichment of genes involved in iron-dependent processes, most notably steroid hormone biosynthesis (Tables 1, 2). The results for *IRP1B^{3R3Q}* were very similar (Pearson correlation 0.896, $P < 0.001$), and will not be discussed separately here.

Specifically, six of the seven known Halloween enzymes were found among the 60 most strongly downregulated genes. Furthermore, other genes involved in ecdysone biosynthesis, such as transcription factors, sterol transporters, heme biosynthesis, and iron-sulfur cluster assembly proteins were also significantly enriched in this set (Table 2). Remarkably, the fold changes for these genes were highly consistent with the predicted functions of these IRP1A variants. In particular, wild type IRP1A displayed the same trend as *IRP1A^{3R3Q}*, but fold changes were less severe. This is consistent with the idea that wild type IRP1A is still capable of binding to mRNAs, effectively reducing nuclear IRP1A levels, resulting in similar, but reduced responses. *IRP1A^{C450S}* is mostly cytoplasmic, but interacted weakly with histones (Supplementary Data 1), suggesting some nuclear presence. However, most gene expression changes were not significant, suggesting that *IRP1A^{C450S}* had little influence on altering the expression profiles of this gene set. In conclusion, the use of different IRP1A variants allowed us to distinguish the different subcellular roles of IRP1A, and we could show that *IRP1A^{3R3Q}*, but not *IRP1A^{C450S}*, dramatically and significantly altered the expression of genes involved in iron-dependent processes.

Discussion

In this report, we demonstrated that the *Drosophila* glycogen branching enzyme, *AGBE*, has hitherto undiscovered and essential roles in the regulation of cellular iron homeostasis. We expect that *AGBE*'s role in iron is not limited to the PG since genome-wide expression profiling indicates that *AGBE* is widely expressed²⁹. While *AGBE* has not been directly linked to iron homeostasis, a possible indirect link exists because mutations in *RBCK1* (RanBP-type and C3HC4-type zinc finger-containing protein 1), a gene that encodes an E3 ubiquitin ligase, cause Polyglucosan Body Myopathy, a recently described glycogen storage disorder³⁰. Intriguingly, *RBCK1* was shown to control cellular iron homeostasis by degrading the oxidized form of IRP2³¹, raising the idea that glycogen and iron processes are linked on multiple levels.

The finding that *AGBE* regulates cellular iron homeostasis led to another surprising discovery, namely that IRP1, in a tissue-specific manner, enters nuclei in its holoform to transcriptionally downregulate iron-intensive processes. Further, both *AGBE* and IRP1A interact with *Cisd2*, a close homolog of vertebrate mitoNEET, which is known to repair oxidatively damaged IRP1. We conclude that the glycogen metabolism enzyme *AGBE* has a “moonlighting” function in aiding *Cisd2* in this repair process, and that loss of either *Cisd2*- or *AGBE*-function results in the accumulation of damaged IRP1A, which interferes with nuclear entry (Figs. 3f, 4j, 5) and IRP1A aconitase activity (Supplementary Fig. 7C). This is consistent with our finding that only holo-IRP1A can translocate to nuclei since both BPS-treatment and a mutation in a critical cysteine required for Fe-S binding (*IRP1A^{C450S}* and *IRP1B^{C447S}*) impairs nuclear access (Fig. 3d).

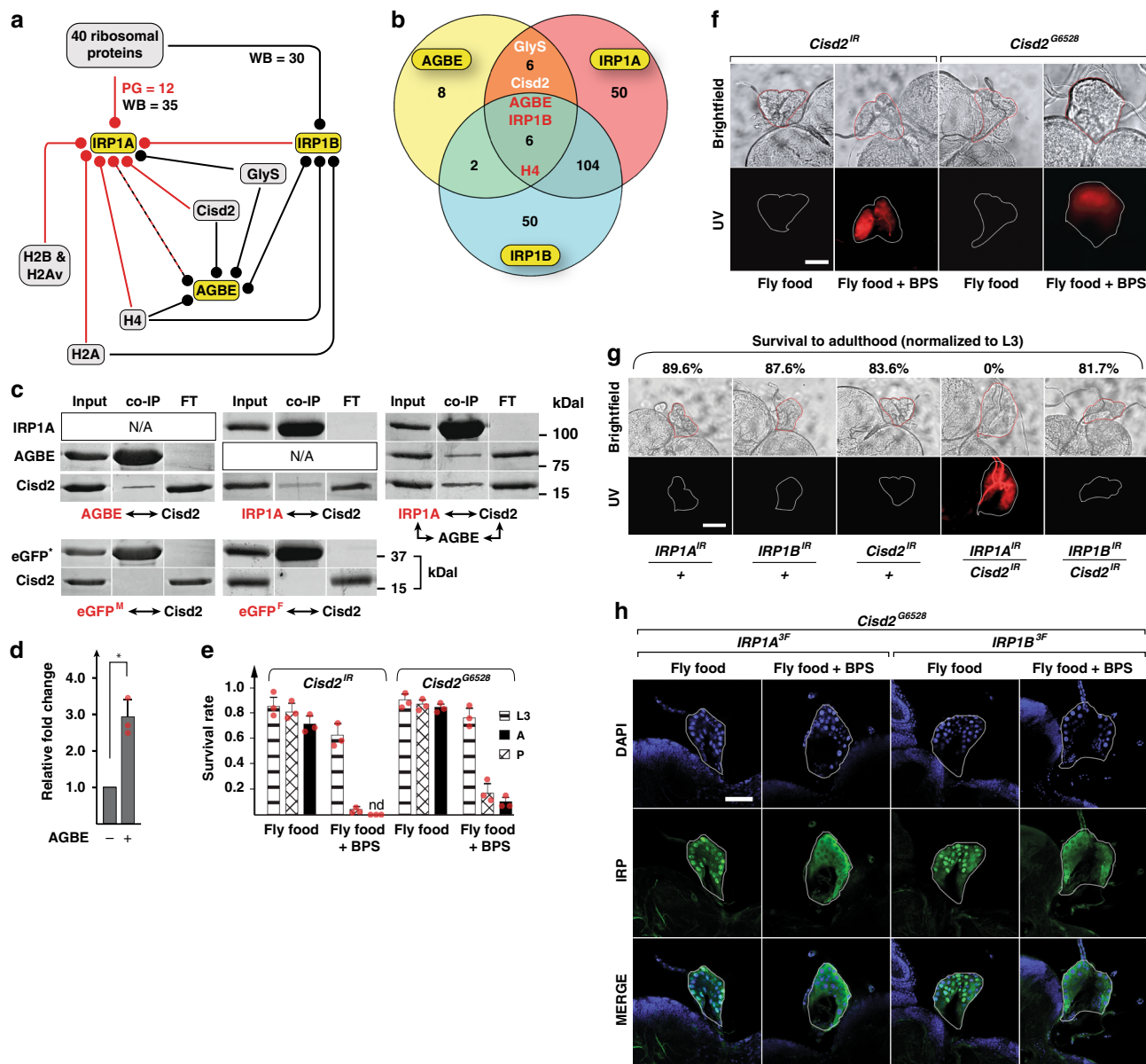


Fig. 4 Cisd2 interacts with IRP1A and AGBE. **a** Protein-protein interaction map. Lines carrying knock-in alleles encoding Flag-tagged AGBE, IRP1A and IRP1B (yellow boxes, Supplementary Fig. 4) were used to produce bait (circle) for immunoprecipitation followed by mass spectrometry (MS) to identify physically bound proteins to the bait. Whole-body (WB, black) and prothoracic gland samples (PG) were used. Red: detected in both PG and WB samples. Dashed line: Only WB samples were tested for AGBE. H2Av, H2A, H2B and H4 are histone proteins. GlyS = Glycogen Synthase. **b** Venn diagram depicting overlaps of immunoprecipitated proteins from endogenously tagged proteins (WB samples). H4 & GlyS see A. **c** Co-transfection of Schneider 2 cells with plasmids encoding Myc-tagged AGBE, Flag-tagged IRP1A and HA-tagged Cisd2, followed by immunoprecipitation via anti-Myc or anti-Flag antibodies and Western blotting. Names shown in red indicate the protein used as bait. Myc-tagged and Flag-tagged enhanced GFP (eGFP^M and eGFP^F, respectively) served as negative controls. Presence of co-immunoprecipitated proteins were tested with anti-HA antibodies and anti-Myc antibodies. **d** Quantification of immunoprecipitated Cisd2 in the triple co-transfection experiment shown above in C. Graph shows relative fold change of co-immunoprecipitated Cisd2 with Flag-IRP1A as bait in the presence or absence of AGBE. Data was normalized to the amount of Cisd2 protein in the absence of co-transfected AGBE. The asterisk indicates a *P*-value < 0.05 according to the Student's *t* test. Error bars represent standard deviation based on three biological replicates. **e** Survival rates of *Cisd2*^{IR}-RNAi animals and *Cisd2*^{G6528} mutants on fly food ± BPS. nd = not detected. Error bars represent standard deviation from three biological replicates (each sample contained 50 individuals). **f** Autofluorescence/protoporphyrin accumulation in prothoracic glands (PG) of *PG > Cisd2*^{IR} and *Cisd2*^{G6528} larvae reared on fly food ± BPS. Scale bar = 250 μm. **g** Genetic interaction between *Cisd2* and *IRP1A* on regular (=iron-replete) fly food based on autofluorescing PGs and survival of the corresponding RNAi lines. All lines express RNAi via a PG-specific Gal4 driver (*phm22-Gal4 = PG >*). Scale bar = 250 μm. **h** Subcellular localization of Flag-tagged IRP1A and IRP1B proteins expressed from knock-in alleles (Supplementary Table 1) in *Cisd2*^{G6528} mutants reared on fly food ± BPS. For control larvae, see Supplementary Fig. 10. Scale bar = 500 μm. Source data are provided as a Source Data file.

Thus, cells possess two mechanisms by which functional IRP1A can be generated. One is by “de novo” insertion via the Cytosolic Iron-sulfur protein Assembly (CIA) machinery, a highly conserved machinery that assembles and inserts [4Fe-4S] clusters

into client proteins³². Once inserted, cells require a second “maintenance” process via the mitoNEET/AGBE proteins to replace oxidatively damaged clusters with functional units (Fig. 5). This elegantly explains as to why AGBE-loss-of-function

Table 1 Transcriptional responses of expressing *IRP1A* alleles in the prothoracic gland.

Rank (n/234)	Symbol	Description	FC 3R3Q:C	P	FC IRP1A:C	P	FC C450S:C	P
6	<i>dib</i>	Ecdysone biosynthesis/heme binding/P450	-13.7	4.0E-03	-2.4	>0.05	-1.7	>0.05
7	<i>phm</i>	Ecdysone biosynthesis/heme binding/P450	-11.7	1.7E-02	-2.2	>0.05	1.1	>0.05
12	<i>sad</i>	Ecdysone biosynthesis/heme binding/P450	-9.7	3.2E-02	-1.7	1.7E-02	1.2	>0.05
13	<i>Start1</i>	Sterol transport	-9.6	4.7E-03	-3.1	3.3E-02	-2.3	>0.05
15	<i>CG7322</i>	Short-chain dehydrogenase	-9.0	1.4E-02	-1.8	>0.05	-1.1	>0.05
23	<i>Cyp6g2</i>	Heme binding/P450	-7.2	1.7E-02	-1.1	>0.05	-1.2	>0.05
26	<i>spidey</i>	Short-chain dehydrogenase	-7.0	1.8E-02	-1.6	2.9E-02	-1.6	1.6E-02
34	<i>nvd</i>	Ecdysone biosynthesis/iron sulfur cluster	-6.1	1.7E-02	-2.1	8.9E-03	-1.6	>0.05
35	<i>sro</i>	Ecdysone biosynthesis/short-chain dehydrogenase	-6.0	2.1E-03	-4.2	1.3E-02	-1.2	>0.05
41	<i>GstE14</i>	Ecdysone biosynthesis/glutathione S transferase	-5.6	2.8E-02	-2.6	>0.05	-1.4	>0.05
44	<i>ND-15</i>	NADH:ubiquinone oxidoreductase, iron-sulfur subunit 5	-5.2	2.8E-02	-3.3	>0.05	-2.7	8.9E-03
47	<i>ouib</i>	Ecdysone biosynthesis/zinc finger	-4.9	2.4E-02	-2.1	>0.05	-1.8	>0.05
51	<i>spok</i>	Ecdysone biosynthesis/heme binding/P450	-4.8	3.6E-03	-2.4	2.9E-03	-1.2	>0.05
52	<i>scu</i>	Short-chain dehydrogenase/reductase	-4.7	1.1E-02	-1.3	>0.05	1.2	>0.05
55	<i>Cyt-b5</i>	Cytochrome b5-like heme/steroid binding domain	-4.5	4.4E-02	-1.8	>0.05	-1.4	1.0E-02
56	<i>CG17928</i>	Cytochrome b5-like heme/steroid binding domain	-4.5	1.4E-02	-1.8	>0.05	-2.3	3.0E-03
64	<i>Tig</i>	Heme oxygenase-like	-4.2	6.0E-03	-1.7	>0.05	-1.2	>0.05
74	<i>ND-19</i>	NADH:ubiquinone oxidoreductase	-3.9	4.0E-02	-1.5	>0.05	-1.2	>0.05
98	<i>Fdx2</i>	Ferredoxin/iron sulfur cluster assembly	-3.4	1.3E-03	-1.6	>0.05	1.3	>0.05
107	<i>Npc2a</i>	Sterol transport	-3.3	8.4E-03	-1.9	>0.05	-1.6	>0.05
116	<i>Pbgs</i>	Heme biosynthesis	-3.2	6.4E-03	-1.5	>0.05	-1.2	>0.05
125	<i>Npc1a</i>	Sterol transport	-3.1	3.2E-04	-2.3	2.4E-02	-1.2	>0.05
146	<i>Drat</i>	Response to hypoxia	-2.9	1.6E-02	-1.4	>0.05	-1.6	1.1E-02
170	<i>CG31548</i>	Short-chain dehydrogenase/reductase	-2.7	3.1E-02	-1.8	>0.05	-1.4	>0.05
173	<i>CG32857</i>	Nfu1 homolog/iron sulfur cluster assembly	-2.7	3.7E-02	-1.2	>0.05	-1.2	>0.05
184	<i>ance</i>	Ecdysone biosynthesis/zinc finger	-2.7	3.7E-02	-2.0	>0.05	-1.2	>0.05
202	<i>Alas</i>	Heme biosynthesis	-2.6	1.5E-02	-1.0	>0.05	12.9	2.6E-04
212	<i>CG12056</i>	Cytochrome b5-like heme/steroid binding domain	-2.6	1.7E-02	-1.5	>0.05	1.1	>0.05
218	<i>CG2254</i>	Short-chain dehydrogenase/reductase	-2.6	6.7E-03	1.2	5.1E-05	-1.1	>0.05
221	<i>Vhl</i>	Response to hypoxia	-2.6	2.0E-02	-1.6	>0.05	1.1	>0.05

RNA-Seq analysis of prothoracic gland (PG) samples with PG-specific expression of *IRP1A*^{3R3Q} (non-RNA-binding and nuclear), wild type *IRP1A* and *IRP1A*^{C450S} (constitutively RNA-binding and largely cytoplasmic) transgenes (Supplementary Table 1). A total of 234 genes were significantly downregulated by *IRP1A*^{3R3Q} expression, using a cutoff of -2.5-fold and $P < 0.05$. The fold changes (relative to control = C) and P -values (t -test) are shown for all three conditions and sorted by relative fold changes of *IRP1A*^{3R3Q} vs. controls. For all 234 genes, see Supplementary Data 3, for term enrichment in this set, see Table 2 and Supplementary Data 4

animals can only be rescued by expressing a wild type *IRP1A* transgene, but not by the constitutively RNA-binding form (*IRP1A*^{C450S}): Sustained transgenic expression of wild type *IRP1A* allows cells to produce sufficient functional IRP1A before oxidative damage occurs, simply because the CIA machinery is able to maintain critical levels of holo-IRP1A, despite the absence of a functioning AGBE/mitoNEET repair machinery (Fig. 5). In contrast, *IRP1A*^{C450S} fails to rescue, since it cannot assume the holoform that is required to enter nuclei.

What could be the biological context that requires IRP1A and IRP1B entering the nucleus? In the PG, iron demands are not only exceedingly high, but they also must change dramatically as the need for Halloween enzyme production changes during development (Supplementary Fig. 1 and Fig. 5). It is therefore plausible that once production of ecdysone has peaked, PG cells need to downregulate all processes that are tied to the synthesis of steroids. Since all but one of the ecdysone-producing Halloween enzymes require iron co-factors, it is necessary to downregulate iron-cofactor production in concert with the proteins that require them. We hypothesize that peak levels of bioavailable iron correlate with maximal nuclear activity of holo-IRP1, resulting in a downregulation of iron-dependent processes, in particular,

steroid hormone biosynthesis. As such, holo-IRP1 appears to have a hitherto undescribed role in iron regulation: Apo-IRP1, as a cytoplasmic mRNA-binding protein, responds to a drop in cellular iron and facilitates an increase of bioavailable iron, yet nuclear holo-IRP1 transcriptionally downregulates iron- and heme-dependent processes once peak iron demand is over (Fig. 5).

How does IRP1 cause the coordinated transcriptional downregulation of iron-dependent processes? An attractive model is that IRP1 proteins interact with a subset of modified histone tails, rather than binding to their histone partners in a non-discriminate fashion. We see two possible scenarios from here. First, histone-bound IRP1 could directly recruit repressive chromatin factors such as histone deacetylases or chromatin remodellers and simply act as a co-factor that serves as a readout for cellular iron concentrations. The second and perhaps more intriguing possibility is that holo-IRP1 controls nuclear citrate levels via its aconitase function to indirectly regulate histone acetylation. Nuclear citrate is converted to acetyl-CoA and oxaloacetate by nuclear ATP-citrate lyase (ACL), a metabolic enzyme with critical roles in histone acetylation³³. Acetyl-CoA is the principal substrate for histone acetylation and is considered a

Table 2 Term enrichment analysis via DAVID tools.

Category	Term	P	E
KEGG	Insect hormone biosynthesis	9.9E-07	17.8
Keywords	Oxidoreductase	2.9E-06	2.8
Biological Process	Ecdysone biosynthetic process	5.1E-05	22.5
InterPro	NAD(P)-binding domain	2.5E-04	3.9
Cellular Component	Mitochondrion	4.0E-03	2.1
InterPro	Short-chain dehydrogenase/reductase, conserved site	9.0E-03	9.1
Keywords	Iron	4.0E-02	2.5
InterPro	Cytochrome b5-like heme/steroid binding domain	4.0E-02	9.3
Molecular Function	Iron-sulfur cluster binding	4.0E-02	8.9
Molecular Function	Heme binding	4.6E-02	2.7
Keywords	Metalloprotease	6.2E-02	4.4
Biological Process	Positive regulation of ecdysteroid biosynthetic process	9.8E-02	19.5

We analyzed 234 genes (see Table 1) for GO terms (Biological Process, Molecular Function, Cellular Component), keywords, Kegg pathway terms, and InterPro protein domains. *P* = *P*-value (based on EASE Score, a modified Fisher Exact *P*-Value), *E* = fold enrichment. For full GO results, see Supplementary Data 4

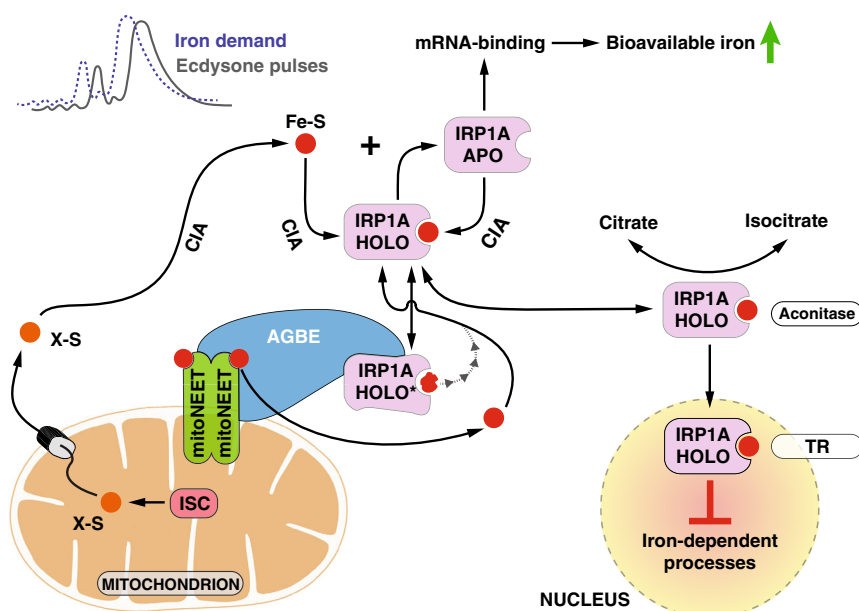


Fig. 5 Model for AGBE-mitoNEET/Cisd2-IRP1A function in tissues with dynamic iron requirements. In *Drosophila*, iron demand peaks prior to maximal ecdysone production to equip ecdysone-synthesizing enzymes with iron cofactors. Newly synthesized IRP1A receives Fe-S clusters (red circles) from the Cytosolic Iron-sulfur cluster Assembly (CIA) machinery, which produces [4Fe-4S] sulfur clusters from an unidentified mitochondrial precursor molecule, X-S (produced in mitochondria by ISC = Iron-Sulfur Cluster Assembly Machinery). Oxidatively damaged IRP1A (IRP1A-HOLO*) requires the mitoNEET/Cisd2 and AGBE proteins to replace impaired clusters with functional units. Holo-IRP1A is both needed for the aconitase function as well as nuclear entry. Loss of AGBE or mitoNEET/Cisd2 function results in a depletion of holo-IRP1A, and the concomitant loss of nuclear IRP1A, explaining why *AGBE* mutants cannot be rescued with the IRP1A^{C450S} form, which only assumes the apo-form since it cannot incorporate an Fe-S cluster. The model suggests that once iron demand has peaked and nuclear holo-IRP1A levels become maximal, the protein acts to throttle expression of genes acting in steroid, heme and iron metabolism in anticipation of falling iron demands. As such, IRP1A has two functions: 1. As known from mammalian cells it acts in response to low cellular iron levels as an RNA-binding protein that promotes increased iron availability, and 2. as a new function, it responds to peak iron levels as a nuclear protein to promote downregulation of processes depending on iron and heme (TR = Transcriptional Regulation).

highly regulated nuclear metabolite that controls histone acetylation status^{34,35}. Histone-bound IRP1A and IRP1B could then act by converting citrate into isocitrate and deplete Acetyl-CoA levels, thus negatively impacting gene expression by promoting histone de-acetylation.

Mutations in human GBE1 cause Andersen disease, also known as Glycogen Storage Disease Type IV (GSD IV)³⁶, but the gene has not been linked to iron homeostasis yet. There are strong indications, however, that GBE1 has hitherto undocumented roles in vertebrate iron metabolism as well. Besides the

earlier mentioned interaction with IRP1, GBE1 was identified by whole-exome sequencing as a novel mitochondrial disorder locus³⁷, consistent with a study that found abnormal mitochondria in GSD IV patients³⁸. Furthermore, GBE1 is transcriptionally upregulated in response to hypoxia and one of the most strongly induced genes upon nickel exposure³⁹⁻⁴¹. Nickel exposure elicits hypoxic responses, and at least in vertebrates, hypoxia and iron metabolism are tightly linked⁴². Perhaps most intriguingly, Nrf2, a transcription factor controlling mitochondrial biogenesis and important iron metabolism genes, was shown to bind directly to

the GBE1 promoter^{43,44}, raising the idea that this glycogen enzyme is coordinately controlled with other key iron genes. Taken together, our findings strongly suggest that the disease etiology of GSD IV needs to be re-assessed from the perspective that GBE1 has a key role in cellular iron homeostasis, and that there must be a re-evaluation of current therapeutic strategies in the future.

The loss-of-function phenotypes for *Cisd2*/mitoNEET, AGBE, and IRP1A are very similar since they display protoporphyrin accumulation that disappears under iron-replete conditions. This is consistent with the idea that depleting *Cisd2*/mitoNEET or AGBE equates the loss of IRP1A function, as both appear to act in concert to replace damaged Fe-S clusters in IRP1A. We have shown that IRP1A is an essential protein required for responding to low dietary iron levels, but *IRP1A* null mutants survive on an iron-rich diet. Therefore, our data strongly suggests that *Cisd2*/AGBE are gatekeepers that ensure proper functioning of IRP1A, a function that becomes non-essential in iron-replete conditions. Vertebrates encode three mitoNEET-like proteins, *Cisd1-3*²³. *Drosophila* lacks a direct *Cisd1* orthologue but harbours copies of *Cisd2* and *CG3420* (*Cisd3*). Of the two, *Cisd2* is more similar to Naf-1 and mitoNEET⁴⁵. We were unable to identify any defects when disrupting *CG3420* function via RNAi (not shown), suggesting that *Cisd2* is the functional equivalent of mitoNEET in *Drosophila*. The fact that a) fly *Cisd2* interacts physically and genetically with IRP1A and b) that mutations in either gene resulted in comparable phenotypes strongly supports the notion that IRP1A function depends on *Cisd2*, consistent with the finding in vertebrates that mitoNEET is involved in repairing oxidatively damaged Fe-S clusters. Similar to *Drosophila* IRP1A, null mutations of mouse *IRP1* or *IRP2* are non-lethal under normal conditions, however, the double knockout is embryonic lethal^{46–50}. *IRP1* null mutants exhibit increased blood haemoglobin levels (polycythemia)^{46,48,50} and one lab reported⁴⁸ that these mice developed also pulmonary hypertension that was exacerbated by exposure to a low iron diet, causing premature death.

The existing parallels between vertebrate IRP1 and *Drosophila* IRP1A raise the interesting question as to whether vertebrate IRP1 has a nuclear role as well, and whether it is conceivable that such a function has been hitherto overlooked. Consistent with this idea, a search of a human protein–protein interaction database¹⁵ found that IRP1 interacts with Histone 2Ab⁵¹ (out of 19 reported proteins in total). In addition, we found that the presence of IRP1A in nuclei varies with tissue and nutritional conditions, raising the possibility that nuclear translocation occurs only under certain circumstances. This may be controlled by physiological parameters, depending on whether a tissue has high or normal iron requirements, and may be temporally regulated during development, as is the case for the PG. Further, we showed that the vertebrate IRP proteins use the same principles as their *Drosophila* counterparts for nuclear entry since only human IRP1 has the ability to translocate to *Drosophila* nuclei, while IRP2, which lacks an Fe-S cluster, does not. It should also be noted that our findings were aided by the fact that the tissues we investigated are polytene, and consequently harbour, compared to most human cells, very large nuclei that allow easy visualization of nuclear proteins. Finally, we searched the literature for studies that had examined the subcellular localisation of IRP1 in more detail. To the best of our knowledge, the existing data relies solely on cell culture experiments with SW1088 and HepG2 cells, which reported IRP1 to mainly reside in the cytosol, but also found IRP1 associated with the endoplasmic reticulum and the Golgi apparatus^{52,53}. While the effects of hypoxic and iron-deprived conditions on IRP1 localisation were tested, iron-rich conditions were not. Taken together, we believe that IRP1, at least in certain circumstances, behaves like its *Drosophila* counterpart, and enters

nuclei where it is physiologically relevant. Future studies will have to revisit this issue in vertebrates.

Methods

Drosophila stocks and husbandry. We obtained the following stocks from the Bloomington *Drosophila* Stock Center: *w¹¹¹⁸* (#3605), *UAS-AGBE^{IR2}* (#42753), *Cisd2^{G6528}* (#30170), *Tubulin-Gal4/TM3 Ser.GFP* (#5138), *UAS-eGFP* (#5431), *UAS-FLP* (#4539), *UAS-CD8.Venus* (#65609), *Vas.Cas9* (#51323). Stocks *UAS-AGBE^{IR1}* (#108087), *UAS-IRP1A-RNAi* (#105583), *UAS-IRP1B-RNAi* (#110637), *UAS-Cisd2-RNAi* (#104501) were obtained from the Vienna *Drosophila* Resource Center. We used CRISPR/CAS9 to generate the following knock-in and knock-out alleles (see Supplementary Fig. 4 for details): *AGBE^{FCF}*, *AGBE^{FCM}*, *IRP1A^{3F}*, *IRP1A^{C450S.3F}*, *IRP1A^{3R3Q.3F}*, *IRP1B^{3F}*, *IRP1A^{FCF}/TM3 Ser.GFP*, *IRP1A^{KO}/TM3 Ser.GFP*, *IRP1B^{KO/KO}*. We also generated transgenic lines based on the PhiC31 system: *UAS-3xFlag-IRP1A^{WT}*, *UAS-IRP1A^{WT}*, *UAS-3xFlag-IRP1A^{C450S}*, *UAS-IRP1A^{C450S}*, *UAS-3xFlag-IRP1A^{3R3Q}*, *UAS-3xFlag-IRP1B^{WT}*, *UAS-IRP1B^{WT}*, *UAS-3xFlag-IRP1B^{C447S}*, *UAS-IRP1B^{C447S}*, *UAS-3xFlag-IRP1B^{3R3Q}*, *UAS-Yeast Aco1^{WT}*, *UAS-Yeast Aco1^{ΔSp}*, *UAS-3xFlag-hIRP1^{WT}*, *UAS-3xFlag-hIRP2^{WT}*, *dU6-3-IRP1A^{gRNA}* (Supplementary Table 1). *y¹w⁺P^{nos}-PhiC31.NLS;[X]; P[carryP]attP40(II)* and *y¹w⁺P^{nos}-PhiC31.int.NLS[X]; P[carryP]attP2(III)* were gifts from BestGene Inc. *Phm22-Gal4* was a kind gift from Michael O'Connor's lab. Stocks were maintained on a standard cornmeal diet unless otherwise specified.

Survival studies. Regular fly food refers to “NutriFly”-based media, which follows the standard recipe from the Bloomington *Drosophila* Stock Center (<https://bdsc.indiana.edu/information/recipes/bloomfood.html>). Flies were reared at 25 °C and 60–70% humidity. Prior to any fly-based experiments, stocks were reared on NutriFly media for at least two generations. Modified media were prepared by adding compounds (e.g., iron) during the preparation process. For iron-enriched media, a 1 M stock solution of Ferric Ammonium Citrate (FAC) (Sigma #F5879) was used to make NutriFly containing 1 mM FAC. For iron-depletion media, NutriFly containing 100 μM BPS (Sigma #146617) was prepared. For egg collections, flies were allowed to lay eggs for 3 × 1 h in order to reduce egg retention and minimize the presence of old embryos. For each vial, 50 embryos were then collected in 1-h intervals. Embryos were counted and transferred to vials containing appropriate media. Larval survival was scored for every stage. At least three independent crosses (=three biological replicates) were carried out per experimental condition.

Construction of transgenic lines. For transgene properties, see Supplementary Table 1. cDNAs were obtained from the *Drosophila* Genomic Resource Center (*AGBE*: #RE12027, *IRP1A*: #LD36161, *IRP1B*: #LD13178, *Cisd2*: #RE49709). Human *IRP1* cDNA (#HG10966-UT) and human *GBE1* cDNA (#HG18919-UT) were acquired from Sino Biological Inc, while the human *IRP2* cDNA (#OHS1770-202318020) was obtained from Dharmacon. To generate equivalent expression of transgenic constructs, we used PhiC31 vectors pBID-UASC-FG (Addgene #35201) and pBID-UASC-G (Addgene #35202) to ensure insertion into the same locus⁵⁴. Vector backbones were amplified via PCR to generate two fragments per vector and fused to cDNA fragments via the Gibson reaction. Mutations were generated via Q5 mutagenesis PCR (NEB #M0491S) following the manufacturer's instructions. Fused fragments were cloned into DH5a *E. coli* competent cells, and validated by Sanger sequencing. For primers see Table 3.

Generation of CRISPR/CAS9 fly lines. We identified optimal target gRNA sites by relying on comparable results from two independent programs, “CRISPR Optimal Target Finder” (University of Wisconsin; <http://tools.flycrispr.molbio.wisc.edu/targetFinder/index.php>) and Harvard's “Find CRISPR” sgRNA design tool (<http://www.flyrnai.org/crispr/index.html>)⁵⁵. Target sites were confirmed by sequencing corresponding loci in the *Vas.Cas9* line (Bloomington #51323) that we used for embryo injections. CRISPR lines were generated via CRISPR/Cas9 homology-directed repair to replace endogenous alleles. Plasmids carrying gRNA target sites were cloned into pCFD3 (Addgene #49410) for *AGBE^{FCF}*, *AGBE^{FCM}*, *IRP1A^{3F}* and *IRP1B^{3F}* constructs, or pCFD5^{56,57} (Addgene #73914) for *IRP1A^{KO}*, *IRP1A^{FCF}* and *IRP1B^{KO}*. All donor template fragments were amplified from genomic DNA via PCR and cloned into the pDsRed-attP vector (Addgene #51019)⁵⁷. For primers see Table 3.

Embryo injection. PhiC31 constructs were injected at 500–600 ng/μl concentrations, while CRISPR plasmids were used at a concentration of 100–150 ng/μl for the double gRNA plasmid and 500–600 ng/μl for the donor template. Injections were performed either at the University of Alberta or via GenetiVision Corporation using standard procedures. 300–500 embryos were injected per construct. Surviving adults were backcrossed to *w¹¹¹⁸* and used to generate independent lines.

Immunostaining. Brain-ring gland complexes (BRGC) were isolated from (unless stated otherwise) 40–42 h 3rd instar larvae and transferred to 1 × PBS. Samples were fixed in 1 × PBS 4% formaldehyde (ThermoFisher #28906) for 20 min at room temperature (RT) followed by washing in 1 × PBS 0.3% Triton (Sigma #T9284)

Table 3 Primer sequences.

Primer name	Primer sequence (5'-3')
Generation of transgenic cDNA lines	
attB1 IRP1A FP	CAAGTTTGTACAAAAAAGCAGGCTATGTCCGGCTCCGGCGCCAATC
attB2 IRP1A RP	TCCACTTTGTACAAGAAAGCTGGGTCTAATCCAGCATTTTGGGTATC
attB1 IRP1B FP	TCAAGTTTGTACAAAAAAGCAGGCTATGTCAGGCGCCAATCCCTTC
attB2 IRP1B RP	CCCACCTTTGTACAAGAAAGCTGGGTTTAAAGAGAGCATTTTGCGAATCATG
attB1 yeast Aco1 DelSp FP	CCAAGTTTGTACAAAAAAGCAGGCTGTCTCCAACCTGACTAGAGATTG
attB2 yeast Aco1 RP	CACTTTGTACAAGAAAGCTGGGTTTTCTTCTCATCGGCTTAATTTTAAAG
attB1 yeast Aco1 WT FP	CCAAGTTTGTACAAAAAAGCAGGCTATGCTGTCTGCACGTTCTG
attB1 human IRP1 FP	CAAGTTTGTACAAAAAAGCAGGCTATGAGCAACCCATTGCGAC
attB2 human IRP1 RP	CCCACCTTTGTACAAGAAAGCTGGGTCTACTTGGCCATCTTGGCGATC
attB1 human IRP2 FP	TCAAGTTTGTACAAAAAAGCAGGCTATGGACGCCCAAAAGCAG
attB2 human IRP2 RP	TCCACCTTTGTACAAGAAAGCTGGGTCTATGAGAATTTTCTGTGCCAC
attB1 FG RP	AGCCTGCTTTTTTGTACAAAACCTTGATACCGGTGCTTGTGCATCGTC
miniwhite FP	GAGTTCGATGTGTTTATAAGGGTATCTAGCATTAC
miniwhite RP	GTAATGCTAGATACCTTAATAAACACATCGAACTC
attB2 FG FP	ACCCAGCTTTCTTGTACAAAAGTGGAGACGTAAGCTAGAGGATCTTTGTG
attB1 UASCG RP	AGCCTGCTTTTTTGTACAAAACCTTGAGATATCGAGCTCTCCGGAATTCGGATC
attB2 UASCG FP	ACCCAGCTTTCTTGTACAAAAGTGGAGATATCGCATGCGGTACCTC
Yeast Aco1 WT RevMut FP	ATGCTGTCTGCACGTTCTGCATCAAGAGACCCATTGTCGTGGTCTTGCACAGTCTCAACTGACTAGAGATTC
Mutagenesis of <i>IRP1A</i> variants	
IRP1A C450S Mut FP	ATCACCTCGAGCACGAACACTTC
IRP1A C450S Mut RP	GGCGGCAATCACAAAGATC
IRP1A R549Q Mut FP	CGGGCAATCAGAAATTCGAG
IRP1A R549Q Mut RP	ACAGGACGCCACAGCAAAC
IRP1A R554Q Mut FP	ATACTAGGGCCAATTACTGGCCAG
IRP1A R554Q Mut RP	TGGGATGGATCTGACCTC
IRP1A R712Q Mut FP	CTATTTGTGCGAACAGGGTCTAACGCCGCGCGAC
IRP1A R712Q Mut RP	CGCGCTGCCGGTGACTTTCTGTG
IRP1A R793Q Mut FP	TGGCAGCTCACAGGATTGGGCCGCAAG
IRP1A R793Q Mut RP	CTGCCGTAGTCTTGCCTAC
Mutagenesis of <i>IRP1B</i> variants	
IRP1B C447S Mut FP	TCACATCCAGCACGAACACATC
IRP1B C447S Mut RP	TGGCCGCAATGACAACAGATC
IRP1B R546Q Mut FP	AGTTTTGTCCGGAACCAGAACTTCGAG
IRP1B R546Q Mut RP	CCAGCACACACGAGGCCGTTCTTCTCGATG
IRP1B R551Q Mut FP	CAACTATCTGGCCAGTCTCTG
IRP1B R551Q Mut RP	GCCCTGGTGTGGGATGGATCTGACCTCGAAG
IRP1B R709Q Mut FP	TCTTGTCCGAGCAGAACATCACACCCCGTG
IRP1B R709Q Mut RP	ATCGGGCAGCAGCGAGGTTCTAG
IRP1B R790Q Mut FP	CGGAAGCTCTCAGGATTGGGCCGCAAG
IRP1B R790Q Mut RP	CTGCCGTAGTCTTGCCTAC
Generation of AGBE CRISPR lines	
AGBE LA FP	CGCTGAAGCAGGTGGAATTCTATGGCAACAGTCCGGTGGCTTCTG
AGBE FRT LA RP	GAAGTTCCTATACTTTCTAGAGAATAGGAACCTCGGAAACAGCTCTGCTCCACTG
AGBE FRT Middle FP	GAAGTTCCTATTCTCTAGAAAGTATAGGAACCTCGAGTGGCGCACTAATCTGTG
AGBE 3xFlag RP	AATATCATGATCCTTGTAGTCTCCGTCGTGGTCCCTATAGTCCATCTAGTCACTGACCGGGCATAAAC
AGBE 3xFlag_3UTR FP	ACTACAAGGATCATGATATTGATTACAAAGCAGATGACGATAAGTAGTCTAGTCACTGACCGCAATTAAC
AGBE 3UTR RP	ACTACGATCGCAGGTGTGCAAAAGCAAGCCAAATCCCTAAAATTC
AGBE RA FRT FP	ACTCATCAATGTATCTTAGAAGTTCCATTTCTAGAAAAGTATAGGAACCTC CATTGGCCAATAACAAAG
AGBE RA RP	TGCATGGAGATCTTTACTAGCATTTAGTTCTGCTCTCTTTGTTG
AGBE 3xMyc RP	TGCTCGAGGTCTCCTCGGAGATGAGCTTTTGTCTCAAGATCCTTTCAGAAATAAGTTTTTGTCTCTAGTCACTGAC
AGBE 3xMyc_3UTR FP	GCGGGCATAAAC
pCFD3 AGBE Left gRNA FP	TCCGAGGAGGACCTCGAGCAGAAGTTGATCAGCGAGGAAGACTTGTAGCTAGTCACTGACCGCAATTAAC
pCFD3 AGBE Left gRNA RP	GTCGGAGCAGAGCTGTTTCCGAG
pCFD3 AGBE Right gRNA FP	AAACTCGGAAACAGCTCTGCTCC
pCFD3 AGBE Right gRNA RP	GTCGGATTTGGGCTTGTCTTCAT
pCFD3 AGBE Right gRNA RP	AAACATGAAAGCAGCCCAATC
Generation of <i>IRP1A</i> ^{KO} CRISPR line	
IRP1A LA FP	TGTCGCCCTTCGCTGAAGCAGGTGGGTACGAGTGGGCGGGACAGAAG
IRP1A KO LA RP	GCACTACGATCGCAGGTGTGCATATAGTGAATAATTTATCATTTTTGTGATTC
IRP1A KO RA FP	TATACGAAGTATAGAAGAGCGCAAACCCAGTCTGCTAAAAATGCCTAAC
IRP1A RA RP	GATTGACGGAAGAGCCTCGAGCGCTGGTGGTGTGGTGTGTTGCTG
pCFD5 IRP1A Left gRNA FP	CGGCCCGGGTTCGATTCGCCGCGATGCAAGAAACATTTGTAAATATAG GTTTTAGAGCTAGAAAATAGCAAG
pCFD5 IRP1A Right gRNA RP	ATTTTAACTTGCTATTTCTAGCTCTAAAACATGGCCAAACCAGTCTGCTTGACCAGCCGGGAATCGAACC
Generation of <i>IRP1A</i> ^{3F} CRISPR line	
IRP1A 3 F LA FP	CCCTTCGCTGAAGCAGGTGGTACCTCGGTTTCGGGGCCCAAG
IRP1A 3 F LA RP	GATCCGGCTGGCGAGATGTGGTGGTGGTCACTGAATCACCGAG
IRP1A 3 F Middle FP	CTCGGTGATTCAAGTACCACCCAGCACATCTCGCCAGCCGATC
IRP1A 3 F 3xFlag RP	CTTGTAATCGATGTCATGATCTTTATAATCACCCTCATGGTCTTTGTAGTCACTCCAGCATTTCGCGTATCATATAG
IRP1A 3 F 3xFlag FP	AGATCATGACATCGATTACAAGGATGACGATGACAAGTAGTGTAGTGCCTTCGTTGACTTTTATATTC
IRP1A 3 F Middle RP	CGATCGCAGGTGTGCATAGTAAAGCATTGTTAGCAG
pCFD3 IRP1A 3 F Left gRNA FP	GTCGGCTGGCGAGATGTGGTCCG
pCFD3 IRP1A 3 F Left gRNA RP	AAACCGACCACATCTCGCCAGCC
pCFD3 IRP1A 3 F Right gRNA FP	GTCGAGCAGGACTGGTTTGGCCAT
pCFD3 IRP1A 3 F Right gRNA RP	AAACATGGCCAAACCAGTCTGCT
Generation of <i>IRP1A</i> ^{C450S,3F} and <i>IRP1A</i> ^{3R3Q,3F} CRISPR lines	
IRP1A CRISPR Mut LA FP	TGGAATCTTGCATGCTAGCGTGACAACCTTTCATGTGCTG
IRP1A CRISPR Mut LA RP	TGGATATCAAGTAATAAATTTAGATAATTTTAAAG
IRP1A CRISPR Mut Middle FP	TGGATGTGGATCATTAGATCGCTCCGAGAAGAAAATCGATATTATCCGGAAG
IRP1A CRISPR Mut Middle RP	GCACTACGATCGCAGGTGTGCATAGTAAAGCATTGTTAGCAGGACTG
IRP1A CRISPR Mut RA RP	TGTATGCTATACGAAGTTATAGAAGAGCGCTGCTGGTGAATCATCGACAAG

Table 3 (continued)

Primer name	Primer sequence (5'-3')
IRP1A CRISPR Mut RA FP	GATTGACGGAAGAGCCTCGAGCTGCACCTGGTGCTGGTGGTG
IRP1A pCFD5 FP	GCGGCCCGGTTTCGATTCCCGCCGATGCAAATTTACTTACTGATATCCAGTTTTAGAGCTAGAAATAGCAAG
IRP1A pCFD5 RP	ATTTTAACTTGCTATTTCTAGCTCTAAAACATGATTCACCAGCAGCGCTTTGACCAGCCGGGAATCGAAC
Generation of <i>IRP1A^{FCF}</i> CRISPR line	
IRP1A FCF FRT LA RP	GAAGTTCCTATACTTTCTAGAGAATAGGAACCTCTAGTGGAAATAATTTATCATTTTTG
IRP1A FCF FRT Middle FP	GAAGTTCCTATTCTCTAGAAAGTATAGGAACCTCTAAATTTACAAATGTTTCATTTTAAAG
IRP1A FCF FRT Middle RP	GCACACGATCGCAGGTGTGCATAGAAGTTCTATACTTTCTAGAGAATAGGAACCTCCATCGGCATTTCTGCTATC
Generation of <i>IRP1A^{gRNA}</i> CRISPR line	
IRP1A gRNA FP	GCGGCCCGGTTTCGATTCCCGCCGATGCCTTTATCCGGATAGCGTTGT GTTTTAGAGCTAGAAATAGCAAG
IRP1A gRNA RP	ATTTTAACTTGCTATTTCTAGCTCTAAAACCCAGCTCGCGGACAGCATCTGCACCAGCCGGGAATCGAACCC
Generation of <i>IRP1^{BKO}</i> CRISPR line	
IRP1B KO LA FP	TGCCTTCGCTGAAGCAGGTACAGCAGACAGTAAATAC
IRP1B KO LA RP	TACGATCGCAGGTGTGCATAAGTAATCGACAGAGCTCGTCAATC
IRP1B KO RA FP	ACGAAGTTATAGAAGAGCAGGGTGCTTCCGCAAACGAATTG
IRP1B KO RA RP	CTTATGCATGGAGATCTTTACTAGCGTAGAGCATCTGCACCAGATTTTCG
pCFD5 IRP1B Left gRNA FP	CGGCCCGGTTTCGATTCCCGCCGATGCAGAGCTCTGTCTGATTACTGATGTTTTAGAGCTAGAAATAGCAAG
pCFD5 IRP1B Right gRNA RP	ATTTTAACTTGCTATTTCTAGCTCTAAAACCCCGTGGCCACCAGCAACCTGCACCAGCCGGGAATCGAACCC
Generation of <i>IRP1^{B3F}</i> CRISPR line	
IRP1B 3 F LA FP	TGGAATCTTGCTGCTAGCAGCTTCCCATCGATGAGAATACTC
IRP1B 3 F LA RP	GATGCTCTGCAAGAACACATTCTTGCCATTG
IRP1B 3 F Middle FP	CAATGGCAAGAATGTGTTCTTGACAGGACATC
IRP1B 3 F 3xFlag RP	TCCTTGTAATCGATGTCATGATCTTTATAATCACCGTCATGGTCTTTGTAGTCAGAGAGCATTGTCGAATCATGTAGTTG
IRP1B 3 F 3xFlag FP	TATAAAGATCATGACATCGATTGCAAGGATGACGATGACAAGTAAGCAACTCATCTTATTTTG
IRP1B 3 F Middle RP	ACGATCGCAGGTGTGCATAGTGGCCCCACCGCAACCCCTTAAAG
pCFD3 IRP1B 3 F Left gRNA FP	GTCGATGTGTTCTTGACAGGACATC
pCFD3 IRP1B 3 F Left gRNA RP	AAACGATGTCCTGCAAGAACACAT
pCFD3 IRP1B 3 F Right gRNA FP	GTCGGTTGCGGTGGGGCCACGGG
pCFD3 IRP1B 3 F Right gRNA RP	AAACCCGTGGCCCCACCGCAACC
Generation of S2 cells transfection constructs	
attB1 eGFP FP	CAAGTTTGTACAAAAAGCAGGCTATGGTGAGCAAGGGCGAGGAGCTGTTC
attB2 eGFP no stop codon RP	CACCTTGTACAAGAAAGCTGGGTCTTGACAGCTCGTCCATGCCGAG
attB1 ABGE FP	CCAAGTTTGTACAAAAAGCAGGCTATGGCCGAGGCTAAGGACATC
attB2 ABGE no stop codon RP	CACCTTGTACAAGAAAGCTGGGTGTCAGTACGCGGGCATAAAC
ABGE Y314S FP	CTGCGTTTCTTGCTATCCAACTGCGTTG
ABGE Y314S RP	CACCTCGTACTCCACTGAGTTGAAGAGACGACTGTC
attB1 hGBE1 FP	TCAAGTTTGTACAAAAAGCAGGCTATGGCGGCTCCGATGACTC
attB2 hGBE1 RP	CCCACCTTGTACAAGAAAGCTGGGTCAATTCGCGCAGATCCACATTC
attB1 hIRP1 FP	CAAGTTTGTACAAAAAGCAGGCTATGAGCAACCCATTGCGCAC
attB2 hIRP1 RP	CCCACCTTGTACAAGAAAGCTGGGTCTACTTGGCCATCTTGGCGATC
attB1 Cisd2 FP	ACAAGTTTGTACAAAAAGCAGGCTATGGAGCCATATCACATCTG
attB2 Cisd2 RP	ACCACCTTGTACAAGAAAGCTGGGTCTTCTTGATGACAATTGGTC
pAFW attB1 RP	AGCCTGCTTTTTTGTACAAACTTGATACCGGTGCTGTGCATCGTCATC
pAFW attB2 FP	ACCAGCTTTCTTGACAAAGTGGGACGTAAGCTAGCAGGATCTTTG
pAMW attB1 RP	AGCCTGCTTTTTTGTACAAACTTGATACCGGTGCTCGCCATGAGCAG
pAMW attB2 FP	ACCAGCTTTCTTGACAAAGTGGGACGTAAGCTAGCAGGATCTTTG
pAHW attB1 RP	AGCCTGCTTTTTTGTACAAACTTGATACCGGTGCTCGCCATGAGCAG
pAHW attB2 FP	ACCAGCTTTCTTGACAAAGTGGGACGTAAGCTAGCAGGATCTTTG
pAc5 STABLE2 RP	CATGGTGCGGAATCCACCAC
pAc5 STABLE2 FP	GAGGAAGTCTTCTAACATGCGGTGACGTGGAGGAGAATCCCGGCCCT
pAc5 3xFlag FP	TGGTGAATTTCGCCACCATGACTACAAGACCATGACGGTGT
pAc5 3xFlag T2A RP	ACCAGGGCCAGGTTCTCTCGACATCTCCGCAAGTCAGTAGGCTGCCGCTCTTCCGCGCCCACTTTGTACAAGAAAG
pAc5 3xFlag T2A 6xMyc FP	TACTGACTTGCGGAGATGTGCAAGAGAACCCTGGCCCTGGTTCGATATCTCTAGAGCCACCGAGCAAAGCTCATTTC
	TGAAG
pAc5 6xMyc attB2 RP	CGGGATTCTCTCCACGTCACCGCATGTTAGAAGACTTCTCTGCCCTCAAGCCACTTTGTACAAGAAAG
pAc5 6xMyc T2A RP	CGGGATTCTCTCCACGTCACCGCATGTTAGAAGACTTCTCTGCCCTCAAGCCACTTTGTACAAGAAAG
pAc5 3xHA FP	AGGAAGCTTCTAACATGCGGTGACGTGGAGGAGAATCCCGGCCCTGCTAGCTACCCATACGATGTTCTCTGAC
pAc5 3xHA attB2 RP	TCATGTCTGGATCCCTCGAGCCACTTTGTACAAGAAAGCTG
Real-time PCR	
SdhB FP	ACGAGCAGTACCGCAACAT
SdhB RP	GGCCTTGCCCTCTTCTC
ABGE qPCR FP	GGCCGTTGAGCATGAGA
ABGE qPCR RP	CGCTTGGTTTATCTTATTCAGC
rp49 qPCR FP	TTCCTTGACGTGCCAAAAC
rp49 qPCR RP	AATGATCTATAACAAAATCCCTCTGA

A list of primers and their sequences that were used for generating S2 cell constructs, transgenic and CRISPR constructs, PCR-based mutagenesis, as well as for quantitative real-time PCR.

(PBS3T) for 3 × 10 min. Samples were blocked at RT for 1 h in blocking solution (1 × PBS3T 5% normal goat serum (Abcam #ab138478)) and incubated in primary antibody dilution buffer (antibody diluted in 1 × PBS3T and 1% BSA) overnight at 4 °C with gentle shaking. Samples were then washed in 1 × PBS3T for three times with 10 min each, incubated in secondary antibody dilution buffer for 1 h at RT, washed in 1 × PBS3T and 1:50,000 DAPI (Cell Signaling #4083) for three times. Samples were mounted in Vectashield mounting medium (#VECTH1000). Pictures were taken on Nikon Eclipse 80i Confocal C2 + microscope/camera. We used the following antibodies: a monoclonal mouse anti-Flag-tag antibody (Cell Signaling #8146S), a rabbit monoclonal anti-Flag tag antibody (Cell Signaling #14793S), a monoclonal rabbit anti-Myc-tag antibody (Cell Signaling #227S). Primary antibody sera were used at a ratio of 1:400 for endogenously tagged proteins and 1:1000 for

transgenically expressed proteins. Secondary antibodies were obtained from Abcam and used at 1:2000 ratio, including goat anti-rabbit IgG H&L (Alexa Fluor 488) (#ab150077), Alexa Fluor 555 (#ab150078), goat anti-mouse IgG H&L Alexa Fluor 488 (#ab150113), and Alexa Fluor 555 (#ab150114).

Ferric iron staining. This protocol was modified from Perl's staining for iron to reduce background noise, a common issue with iron-staining techniques. 42-h L3 larvae were washed in 1 × PBS for three times and dissected for BRGC. Samples were fixed with 1 × PBS/4% formaldehyde for 20 min at RT. BRGC were washed 1 × 10 min, 1 × 20 min and 1 × 30 min in 1 × PBS/0.3% Triton. Samples were incubated at RT for 1 h in fresh staining solution (2% K₄Fe(CN)₆ + 2% HCl) and

briefly washed in 1× PBS/0.3% Triton for 5 × 2 min. Samples were then incubated in 0.01 Na₂S₂O₈/0.3% H₂O₂ for 30 min at RT and washed 3× 10 min in 0.1 M Phosphate buffer pH 7.0 (57.75 mM Na₂HPO₄ and 42.25 mM NaH₂PO₄). Samples were then incubated for 10 min with fresh intensification buffer (0.1 M phosphate buffer pH 7.0 containing 0.00125% DAB and 0.0025% CoCl₂) to reduce background staining, followed by 3× 10 min wash steps in 0.1 M phosphate buffer pH 7.0. Images were taken using epifluorescence camera (Nikon Digital Sight DS-U3).

RNA-sequencing. Animals were reared on standard NutriFly media (Diamed). For a single biological replicate, 50 ring glands were manually dissected in 1× PBS, transferred to Trizol (ThermoFisher #15596026), and flash-frozen in liquid nitrogen for long-term storage. RNA was extracted with the RNeasy kit (Qiagen #74106) coupled to an on-column DNA digestion step using RNA-free DNase (Qiagen #79254). Extracted RNA was examined on a Bioanalyzer using Agilent RNA 600 nano kit (#5067-1511) to confirm RNA integrity. 100 ng total RNA from each sample was used for generating strand-specific RNA-Seq libraries based on the Ovation *Drosophila* RNA-Seq System 1-16 (Nugen #0350-32). cDNA quality was analysed on a Bioanalyzer using the high sensitivity DNA analysis kit (Agilent #5067-4626). 100 ng cDNA in 25 µl nuclease-free water was used for RNA-Seq analysis (Genome Quebec Innovation Center at McGill University). Sequencing data was analysed using Arraystar 4.0 (DNASTar), MS Access and DAVID GO Tools⁵⁸. All RNA-Seq data has been deposited with GEO (entry # GSE130103).

Ex vivo culturing of ring glands. In the first approach, BRGC were isolated from *w¹¹¹⁸* L3 larvae just after the L2/L3 moult, transferred to culture medium (Schneider insect medium with 10% heat-inactivated FBS, 1% streptomycin-penicillin, 10 µg/ml insulin and 2 µg/ml ecdysone), and incubated at 25 °C. These conditions efficiently mimicked in vivo conditions and allowed physiological functions to be studied for up to 48 h⁵⁹. To reduce available iron, BPS was added to the culture medium at a final concentration of 100 nM. After 24 h, ring glands (50 per replicate) were transferred to Trizol for later qPCR analysis. In a separate approach, S2 cells were maintained under the same conditions, with a starting titer of 1 × 10⁶ cells per ml. After 24 h at 25 °C, 3 ml were used for RNA extraction and qPCR analysis. For the in vivo approach, *w¹¹¹⁸* larvae were initially reared on regular NutriFly food, and after the L2/L3 moult transferred to NutriFly food containing 100 µM BPS. After 24 h, ring glands were dissected and subjected to RNA extraction and qPCR analysis. For primers see Table 3.

Quantitative real-time PCR (qPCR). Extracted RNA (Qiagen RNeasy extraction kit) was reverse-transcribed via ABI High Capacity cDNA synthesis kit (ThermoFisher #4368814). Synthesized cDNA was used for qPCR (QuantStudio 6 Flex) using KAPA SYBR Fast qPCR master mix #Sigma KK4601. For each condition, three biological samples were each tested in triplicate. Samples were normalized to *rp49* based on the $\Delta\Delta C_T$ method, with the exception of RNA-immunoprecipitation, where we normalized results to immunoprecipitated IRP1A protein levels. For primers see Table 3.

Constructs for co-immunoprecipitation (S2 cells). Fragments carrying *Drosophila* AGBE and human GBE1 cDNAs were cloned into pAMW while *Drosophila* IRP1A and human IRP1 cDNAs were cloned into pAFW. The *Drosophila* *Cisd2* cDNA was cloned into pAHW, and eGFP was cloned into pAFW as well as pAMW. This approach allowed for the generation of in-frame tagged cDNAs. We used an approach that allows for the co-expression of two cDNAs that are separated by a viral-derived 2A-like peptide, which is then cleaved post-translationally to yield equal amounts of both proteins⁶⁰. Appropriate pairwise combinations of cDNAs encoding wild type or modified versions of 6x Myc-tagged AGBE cDNA, 6x Myc-tagged human GBE1, 3x Flag-tagged IRP1A, 3x HA-tagged *Cisd2* and 3x Flag-tagged eGFP (the latter served as a control) were cloned into pAc5-STABLE2-Neo (Addgene #32426). For the triple transfection of IRP1A, AGBE and *Cisd2*, 3x Flag-tagged IRP1A was cloned together with 6x Myc-tagged AGBE as well as 3x HA-tagged *Cisd2* into pAc5-STABLE2-Neo, separated by viral-derived 2A-like peptides.

Transfection, co-immunoprecipitation and Western Blotting. Cells were grown in Schneider Insect medium with 10% heat-inactivated FBS, 1% Streptomycin-Penicillin following standard procedures and transfected by the Calcium Phosphate-based method (Invitrogen). Transfected cells were lysed, and Myc-tagged bait proteins were immunoprecipitated using Myc-trap agarose beads (Chromotek Myc-Trap[®]-A). Flag-tagged bait proteins were immunoprecipitated using M2 Flag agarose beads (Sigma-Aldrich #A2220) following instructions of the manufacturer. Pulled-down samples were analysed via Western Blotting. To detect 3x Myc-tagged proteins, monoclonal rabbit anti-Myc-tag antibodies (Cell Signaling #2278S) were used at a concentration of 1:2,500 followed by incubation with a goat anti-rabbit IgG H&L HRP secondary antibody (Abcam #ab97051) at a ratio of 1:10,000. To detect 3x Flag-tagged proteins, monoclonal mouse anti-Flag-tagged antibodies (Cell Signaling #8146S) were used at a concentration of 1:2,500 followed by incubation with Goat anti-mouse IgG H&L HRP secondary antibodies (Abcam #97023) at a ratio of 1:10,000. 3x HA-tagged proteins were

detected using either monoclonal mouse anti-HA-tag antibodies (Abcam #18181) or monoclonal rabbit anti-HA-tag antibodies (Cell Signaling #3724S) both at a ratio of 1:2,500 followed by incubation with either Goat anti-mouse or Goat anti-rabbit IgG H&L HRP as a secondary antibody, respectively, at a ratio of 1:10,000. Blots were scanned for image acquisition with a ChemiDoc imaging system (BioRad). Uncropped scans of all Western Blots are provided in Supplementary Figs. 12–13.

Mass spectrometry of whole larvae. Our whole-body mass spectrometry (MS) approach was adapted from an in vivo cross-linking procedure developed for *Drosophila* embryos^{61,62}. We collected 150–200 L3 larvae (40–42 h after the moult) and washed them 3 × 5 min in 1× PBS. Animals were then incubated in 1× PBS with 0.1% Triton (PBSIT) 2 × 5 min before fixing in fresh fixative solution (1× PBSIT with 0.2% Formaldehyde) for 10 min. The fixing solution was removed and replaced by fresh quenching solution (0.25 M glycine in 1× PBSIT). Animals were washed in 1× PBSIT three times before being flash-frozen in liquid nitrogen for long term storage at –80 °C. Larvae were homogenized in 1 ml of 1× lysis buffer (25 mM Na-HEPES pH 7.5, 75 mM NaCl, 0.5 mM EDTA, 10% glycerol, 0.1% Triton X-100, proteinase inhibitor cocktail (Sigma #11873580001)) using a Dounce homogenizer. Lysates were centrifuged at 16,000 g for 30 min at 4 °C. Protein concentrations of supernatants were determined with the Qubit[™] Protein assay (Invitrogen #Q33212) and served to equalize protein amounts for subsequent co-immunoprecipitation assays. The supernatants were then transferred to spin columns (Chromotek sct-50) and incubated with 40 µl of anti-Flag M2 affinity gel (Sigma #A2220) on a rotating shaker for 2 h at 4 °C. Columns were centrifuged and treated with wash buffer 1 (25 mM Na-HEPES pH 7.5, 75 mM NaCl, 0.5 mM EDTA, 10% Glycerol, 0.1% Triton X-100) and wash buffer 2 (25 mM Na-HEPES pH 7.5, 75 mM NaCl, 0.5 mM EDTA, 10% Glycerol) for three times each. At the last step, 40 µl of loading buffer (0.125 M Tris-HCl pH 6.8, 5% SDS, 0.004% Bromophenol blue, 20% glycerol, 1.43 M β-mercaptoethanol) was added and tubes were incubated at 95 °C for 5 min before collecting samples. Samples were then loaded on a 12.5% SDS-gel, stained with Coomassie Blue and submitted for MALDI-TOF MS analysis (carried out by the Alberta Proteomics and MS Facility, University of Alberta).

In brief, we performed overnight in-gel trypsin digestion following standard procedures. Gel bands were excised and destained twice in 100 mM ammonium bicarbonate (Sigma #09830-500 g)/acetonitrile (Sigma #271004) at a ratio of 50:50 (v/v). Samples were then reduced using 10 mM β-mercaptoethanol (Sigma #M6250) in 100 mM bicarbonate, followed by alkylation in 55 mM iodoacetamide (Sigma #I11490) in 100 mM bicarbonate. After dehydration, a trypsin solution (Promega #V5111) was added to cover the gel pieces at a final concentration of 6 ng/µl, and digested overnight (~16 h) at RT. Tryptic peptides were first extracted from the gel using 97% water/2% acetonitrile/1% formic acid followed by a second extraction using 50% of the first buffer and 50% acetonitrile.

Fractions containing tryptic peptides were resolved and ionized by using nanoflow HPLC (Easy-nLC II, Thermo Scientific) coupled to an LTQ XL-Orbitrap hybrid mass spectrometer (Thermo Scientific). Nanoflow chromatography and electrospray ionization were carried out with a PicoFrit-fused silica capillary column (ProteoPeptII, C18) with a 100 µm inner diameter (300 Å, 5 µm, New Objective). Peptides were loaded onto the column at a flow rate of 3000 nl/min and resolved at 500 nl/min using a 60 min linear gradient from 0 to 45% v/v aqueous acetonitrile in 0.2% v/v formic acid. The mass spectrometer was operated in data-dependent acquisition mode, recording high-accuracy and high-resolution survey Orbitrap spectra using external mass calibration, with a resolution of 30,000 and m/z range of 400–2000. The fourteen most intense multiply charged ions were sequentially fragmented by using collision-induced dissociation, and the spectra of their fragments were recorded in the linear ion trap. After two fragmentations, all precursors selected for dissociation were dynamically excluded for 60 s.

Data were processed using the Proteome Discoverer 1.4 software (Thermo Scientific), and we used the SEQUEST search algorithm (Thermo Scientific) to identify peptides in the UniProt (uniprot.org) *Drosophila* proteome database (ID: UP000000803). For this approach, search parameters including a precursor mass tolerance of 10 ppm and a fragment mass tolerance of 0.8 Da. Peptides contained carbamidomethyl cysteines as static modifications and oxidized methionines and deamidated glutamines and asparagines as dynamic modifications. Minimum acceptance criteria were based on two or more peptides per detected protein, and up to two missed cleavage protease cleavage sites (C terminal sites of lysine and arginine residues) were tolerated for peptide matching. Peptide-to-spectrum matches (PSM) were set to 1. We used the target decoy approach^{63,64} to estimate false discovery rates (FDRs) for peptide matches, with the strict FDR value equalling 0.01 and a relaxed FDR of 0.05. For our analysis, the signal to noise threshold was set to 1.5. The SEQUEST protein raw score was used to calculate the final mass spectrometry score for each detected protein. The raw score represents the sum of (i) matched peptide fragment ion intensities, (ii) the number of total and matched fragment ions, and (iii) the factor that reflects the continuity of a matching ion peptide series for a given protein. SEQUEST then determines the final scores by converting the expected masses of peptide ions into a theoretical spectrum, combined with a calculation that determines the cross-correlation between the theoretical spectrum and the experimental spectrum⁶⁵. In total, we analysed 21 samples representing 17 different conditions, four of which were tested

twice (Supplementary Table 2). The reproducibility of the repeated biological samples ranged from 82.4–98.4% (Supplementary Table 2), while the overlap between equivalent IRP1A and IRP1B variants (e.g., IRP1A^{3R3Q} vs. IRP1B^{3R3Q}) ranged from 63.8% to 66.3%. In total, five control samples were used (Supplementary Table 2). Proteins detected in any of the control samples were removed from experimental results.

Mass spectrometry of the prothoracic gland (PG). For PG-specific MS we separated hand-dissected BRGC into individual cells. We used larvae that expressed Venus-tagged CD8 (*UAS-CD8.Venus*, Bloomington stock #65609) in a PG-specific manner. CD8 localises to the cell membrane, allowing purification of PG cells from unlabelled cells⁶⁶. BRGC were collected in *ex vivo* medium (Schneider insect medium with 10% heat-inactivated FBS, 1% streptomycin-penicillin, 10 µg/ml insulin and 2 µg/ml ecdysone) containing a proteinase inhibitor cocktail (Sigma #1187358001). Dissection times were limited to 1 h to minimize physiological changes. Samples were incubated in 1× PBSIT for 2 × 5 min before being fixed in fresh fixing solution (1× PBSIT containing 0.2% formaldehyde) for 10 min. Fixing solution was removed and replaced by fresh quenching solution (0.25 M glycine in 1× PBSIT). Samples were washed three times in 1× PBSIT, followed by immersion in 1× PBSIT/25% glycerol and flash-frozen in liquid nitrogen for long-term storage at –80 °C. For knock-in derived proteins we collected 1.0 ml containing the equivalent of ~15,000 BRGCs isolated from 40–42 h old L3, while roughly half the amount was used for flies with transgenically produced protein. Samples were removed from –80 °C and thawed gradually for 15 min at –20 °C followed by 15 min at 4 °C until completely thawed. Tissue samples were then incubated in cell dissociation buffer (CMF buffer with 1 mg/ml collagenase, 1 mg/ml papain) for 30 min at 30 °C. The digestion was terminated by adding 4x volumes of CMF to the dissociation reaction. Samples were left at RT for 5 min before being centrifuged at 1000 g for 1 min. Cells were 3× washed in PBSIT and incubated with IgG beads that had been cross-linked with mouse CD8 antibody (#ab82005) for 30 min, followed by three brief washes in PBSIT, and an elution step (0.1 M citrate pH 2.3) to release PG cells from beads. All subsequent steps for protein extraction and immunoprecipitation were as described for whole-body MS. All MS proteomics data have been deposited to the ProteomeXchange Consortium⁶⁷ via the PRIDE⁶⁸ partner repository with identifier #PXD013499.

Quantitative RNA-immunoprecipitation (RIP). Our *in vivo* RIP approach was adapted from different cell culture protocols^{69–71}. As controls, we used *w¹¹¹⁸*, which is the parental strain for our transgenic and mutant lines and thus harbours no tagged genes. To immunoprecipitate IRP1A, we used 3× Flag-tagged CRISPR/Cas9-generated knock-in alleles, namely IRP1A^{3F}, IRP1A^{C450S.3F}, and IRP1A^{3R3Q.3F}, representing tagged wild type, constitutively RNA-binding and non-RNA-binding forms of IRP1A, respectively. We collected 200 L3 larvae (staged at 40 h after the L2/L3 moult) per sample. Larvae were washed for 3 × 5 min in PBS, flash-frozen in liquid nitrogen and stored at –80 °C. Larvae were homogenized in 1 ml lysis buffer (150 mM KCl, 25 mM Tris-HCl pH 7.4, 5 mM EDTA, 0.5% v/v Nonidet P-40, 1× proteinase inhibitor cocktail, 100 U/ml RNase inhibitor (NEB #M0314S) using a Dounce homogenizer. Lysates were centrifuged at 12,000 g for 30 min at 4 °C. Supernatants were transferred and filtered through a 0.45 µm syringe filter (Sigma #CLS431225-50EA). Flow-through samples were incubated with 300 µl equilibrated anti-Flag M2 affinity gel solution on a rotating platform for 4 h at 4 °C followed by centrifugation at 12,000 g for 30 min at 4 °C. The supernatant was removed, and the affinity gel washed in 10x volume of lysis buffer for 2 × 5 min. 5% of the final volume was saved for Western Blotting to determine IRP1A levels to adjust sample input for RIP (Fig. 2c). Western Blots were scanned with the ChemiDoc imaging system (Bio-Rad), and bands were quantified using ImageJ following standard procedures. The remaining 95% was used for Trizol-based RNA extraction followed by qPCR for *SdhB*, which harbours a validated IRE^{72,73}. For primers see Table 3.

Measuring IRP1A and IRP1B aconitase activity (S2 cells). S2 cells were grown in Schneider Insect medium with 10% heat-inactivated FBS/1% Streptomycin-Penicillin and transfected by the Calcium Phosphate-based method (Invitrogen). Transfected cells were lysed, and IRP1 protein levels were evaluated as follows: From each sample, 50% of the lysate was used to immunoprecipitate IRP1A or IRP1B, and proteins were separated via SDS-PAGE. This was followed by Coomassie Blue staining of the gel to evaluate IRP1A and IRP1B protein levels, and cell lysate amounts used for aconitase assays were normalized accordingly. Aconitase activity was determined by measuring the rate of NADPH production via absorbance at 340 nm every 5 min (Aconitase-340™ kit, OxisResearch 21041, DU-730 UV/Vis Spectrophotometer). The absorbance rate was normalized relative to the rate of untransfected S2 cells, which served as a negative control for background aconitase activity.

Measuring IRP1A and IRP1B aconitase activity *in vivo*. We measured aconitase activity from both transgenically produced IRP1 (Supplementary Fig. 7) as well as from knock-in alleles (Fig. 2d). For the former, we collected 200–250 L1 larvae that ubiquitously expressed transgenic IRP1A or IRP1B alleles (*tub-Gal4 > UAS-cDNA*) and washed them 3 × 5 min in 1× PBS. To measure the IRP1 aconitase activity in an *AGBE* mutant background, we generated lines carrying either

transgenic *tub > IRP1A* or *tub > IRP1B* together with transgenic *UAS-FLP-cDNA* and the *AGBE^{FCF}* knock-in allele to remove *AGBE* ubiquitously. For corresponding controls, we used the same combination, except that we replaced *UAS-FLP-cDNA* with a *UAS > eGFP-cDNA* transgene. To evaluate the aconitase activity produced by knocked-in IRP1A alleles, we collected 200 L3 larvae (staged at 42 h after the L2/L3 moult) carrying different IRP1A alleles in an IRP1B null mutant background to eliminate IRP1B aconitase activity. Larvae were homogenized in 1 ml of 1× Lysis buffer (25 mM Na-HEPES pH 7.5, 75 mM NaCl, 0.5 mM EDTA, 10% glycerol, 0.1% Triton X-100, proteinase inhibitor cocktail). To reduce the contribution of mitochondrial aconitase (Acon), we removed the mitochondrial fraction via ultracentrifugation at 20,000 g and 4 °C. We normalized samples based on immunoprecipitated tagged protein levels (i.e., IRP1A variants), which we evaluated via Western Blotting (Fig. 2d, not shown in Supplementary Fig. 7), as described in the quantitative RIP section above. Aconitase activity was determined as described for S2 cells. For the knocked-in CRISPR alleles of IRP1A, we used IRP1B null mutants as controls, which harbour a wild type copy of IRP1A.

Reporting summary. Further information on research design is available in the Nature Research Reporting Summary linked to this article.

Data availability

The source data underlying Figs. 1g–h, 2a–d, 3a, 3c, 4e–g, 4i and Supplementary Fig. 7 are provided as a Source Data file at FigShare (<https://figshare.com/s/eb4451ceae5e0fd926f>) with DOI information <https://doi.org/10.6084/m9.figshare.8001809>. Mass spectrometry proteomics data relating to Fig. 4a, b and Supplemental Tables 3–6 have been deposited with the ProteomeXchange Consortium via the PRIDE partner repository (identifier #PXD013499). RNA-Seq data have been deposited with GEO (<https://www.ncbi.nlm.nih.gov/geo/query/acc.cgi?acc=GSE130103>).

Received: 22 June 2018; Accepted: 22 October 2019;

Published online: 29 November 2019

References

- Lill, R. Function and biogenesis of iron–sulphur proteins. *Nature* **460**, 831–838 (2009).
- Muckenthaler, M. U., Rivella, S., Hentze, M. W. & Galy, B. A red carpet for iron metabolism. *Cell* **168**, 344–361 (2017).
- Anderson, C. P., Shen, M., Eisenstein, R. S. & Leibold, E. A. Mammalian iron metabolism and its control by iron regulatory proteins. *Biochim. Biophys. Acta* **1823**, 1468–1483 (2012).
- Walden, W. E. et al. Structure of dual function iron regulatory protein 1 complexed with ferritin IRE-RNA. *Science* **314**, 1903–1908 (2006).
- Volz, K. The functional duality of iron regulatory protein 1. *Curr. Opin. Struct. Biol.* **18**, 106–111 (2008).
- Papanikolaou, G. & Pantopoulos, K. Systemic iron homeostasis and erythropoiesis. *IUBMB Life* **69**, 399–413 (2017).
- Danielsen, E. T. et al. A *Drosophila* genome-wide screen identifies regulators of steroid hormone production and developmental timing. *Dev. Cell* **37**, 558–570 (2016).
- Ou, Q. et al. The insect prothoracic gland as a model for steroid hormone biosynthesis and regulation. *Cell Rep.* **16**, 247–262 (2016).
- Yoshiyama-Yanagawa, T. et al. The conserved rieske oxygenase DAF-36/ Neverland Is a novel cholesterol-metabolizing enzyme. *J. Biol. Chem.* **286**, 25756–25762 (2011).
- Heinemann, I. U., Jahn, M. & Jahn, D. The biochemistry of heme biosynthesis. *Arch. Biochem. Biophys.* **474**, 238–251 (2008).
- Nagababu, E. & Rifkin, J. M. Formation of fluorescent heme degradation products during the oxidation of hemoglobin by hydrogen peroxide. *Biochem. Biophys. Res. Commun.* **247**, 592–596 (1998).
- Caceres, L. et al. Nitric oxide coordinates metabolism, growth, and development via the nuclear receptor E75. *Genes Dev.* **25**, 1476–1485 (2011).
- Cappellini, M. D., Brancaloni, V., Graziadei, G., Tavazzi, D. & Di Piero, E. Porphyrias at a glance: diagnosis and treatment. *Intern. Emerg. Med.* **5**(Suppl 1), S73–S80 (2010).
- Orhan Akman, H. et al. A novel mouse model that recapitulates adult-onset glycogenosis type 4. *Hum. Mol. Genet.* **24**, 6801–6810 (2015).
- Stark, C. et al. BioGRID: a general repository for interaction datasets. *Nucleic Acids Res.* **34**, D535–D539 (2006).
- Wan, C. et al. Panorama of ancient metazoan macromolecular complexes. *Nature* **525**, 339–344 (2015).
- Lind, M. I. et al. Of two cytosolic aconitases expressed in *Drosophila*, only one functions as an iron-regulatory protein. *J. Biol. Chem.* **281**, 18707–18714 (2006).

18. Philpott, C. C., Klausner, R. D. & Rouault, T. A. The bifunctional iron-responsive element binding protein/cytosolic aconitase: the role of active-site residues in ligand binding and regulation. *Proc. Natl Acad. Sci. USA* **91**, 7321–7325 (1994).
19. Regev-Rudzki, N., Karnieli, S., Ben-Haim, N. N. & Pines, O. Yeast aconitase in two locations and two metabolic pathways: seeing small amounts is believing. *Mol. Biol. Cell* **16**, 4163–4171 (2005).
20. Huynh, N., Zeng, J., Liu, W. & King-Jones, K. A. *Drosophila* CRISPR/Cas9 toolkit for conditionally manipulating gene expression in the prothoracic gland as a test case for polytene tissues. *G3 (Bethesda)* **8**, 3593–3605 (2018).
21. Paraskova, E., Gray, N. K., Schläger, B., Wehr, K. & Hentze, M. W. Ribosomal pausing and scanning arrest as mechanisms of translational regulation from cap-distal iron-responsive elements. *Mol. Cell Biol.* **19**, 807–816 (1999).
22. Muckenthaler, M., Gray, N. K. & Hentze, M. W. IRP-1 binding to ferritin mRNA prevents the recruitment of the small ribosomal subunit by the cap-binding complex eIF4F. *Mol. Cell* **2**, 383–388 (1998).
23. Mittler, R. et al. NEET proteins: a new link between iron metabolism, reactive oxygen species, and cancer. *Antioxid Redox Signal* **30**, 1083–1095 (2018).
24. Lipper, C. H. et al. Cancer-related NEET proteins transfer 2Fe-2S clusters to anamorsin, a protein required for cytosolic iron-sulfur cluster biogenesis. *PLoS One* **10**, e0139699 (2015).
25. Tan, G. et al. His-87 ligand in mitoNEET is crucial for the transfer of iron sulfur clusters from mitochondria to cytosolic aconitase. *Biochem. Biophys. Res. Commun.* **470**, 226–232 (2016).
26. Zuris, J. A. et al. Facile transfer of [2Fe-2S] clusters from the diabetes drug target mitoNEET to an apo-acceptor protein. *Proc. Natl Acad. Sci. USA* **108**, 13047–13052 (2011).
27. Inupakutika, M. A. et al. Phylogenetic analysis of eukaryotic NEET proteins uncovers a link between a key gene duplication event and the evolution of vertebrates. *Sci. Rep.* **7**, 42571 (2017).
28. Ferecatu, I. et al. The diabetes drug target MitoNEET governs a novel trafficking pathway to rebuild an Fe-S cluster into cytosolic aconitase/iron regulatory protein 1. *J. Biol. Chem.* **289**, 28070–28086 (2014).
29. Chintapalli, V. R., Wang, J. & Dow, J. A. Using FlyAtlas to identify better *Drosophila melanogaster* models of human disease. *Nat. Genet.* **39**, 715–720 (2007).
30. Nilsson, J. et al. Polyglucosan body myopathy caused by defective ubiquitin ligase RBCK1. *Ann. Neurol.* **74**, 914–919 (2013).
31. Yamanaka, K. et al. Identification of the ubiquitin-protein ligase that recognizes oxidized IRP2. *Nat. Cell Biol.* **5**, 336–340 (2003).
32. Netz, D. J., Mascarenhas, J., Stehling, O., Pierik, A. J. & Lill, R. Maturation of cytosolic and nuclear iron-sulfur proteins. *Trends Cell Biol.* **24**, 303–312 (2014).
33. Wellen, K. E. et al. ATP-citrate lyase links cellular metabolism to histone acetylation. *Science* **324**, 1076–1080 (2009).
34. Moussaieff, A. et al. Glycolysis-mediated changes in acetyl-CoA and histone acetylation control the early differentiation of embryonic stem cells. *Cell Metab.* **21**, 392–402 (2015).
35. Sutendra, G. et al. A nuclear pyruvate dehydrogenase complex is important for the generation of acetyl-CoA and histone acetylation. *Cell* **158**, 84–97 (2014).
36. Li, S. C. et al. Glycogen storage disease type IV: novel mutations and molecular characterization of a heterogeneous disorder. *J. Inher. Metab. Dis.* **33**(Suppl 3), S83–S90 (2010).
37. Pronicka, E. et al. New perspective in diagnostics of mitochondrial disorders: two years' experience with whole-exome sequencing at a national paediatric centre. *J. Transl. Med.* **14**, 174 (2016).
38. Nolte, K. W., Janecke, A. R., Vorgerd, M., Weis, J. & Schröder, J. M. Congenital type IV glycogenosis: the spectrum of pleomorphic polyglucosan bodies in muscle, nerve, and spinal cord with two novel mutations in the GBE1 gene. *Acta Neuropathol.* **116**, 491–506 (2008).
39. Zhao, J. et al. Nickel-induced 1,4- α -glucan branching enzyme 1 up-regulation via the hypoxic signaling pathway. *Toxicol. Appl. Pharm.* **196**, 404–409 (2004).
40. Pescador, N. et al. Hypoxia promotes glycogen accumulation through hypoxia inducible factor (HIF)-mediated induction of glycogen synthase 1. *PLoS One* **5**, e9644 (2010).
41. Buart, S. et al. Transcriptional response to hypoxic stress in melanoma and prognostic potential of GBE1 and BNIP3. *Oncotarget* **8**, 108786–108801 (2017).
42. Mandilaras, K., Pathmanathan, T. & Missirlis, F. Iron absorption in *Drosophila melanogaster*. *Nutrients* **5**, 1622–1647 (2013).
43. Uruno, A. et al. Nrf2-mediated regulation of skeletal muscle glycogen metabolism. *Mol. Cell Biol.* **36**, 1655–1672 (2016).
44. Kerins, M. J. & Ooi, A. The roles of NRF2 in modulating cellular iron homeostasis. *Antioxid Redox Signal* **29**, 1756–1773 (2017).
45. Hu, Y. et al. An integrative approach to ortholog prediction for disease-focused and other functional studies. *BMC Bioinform.* **12**, 357 (2011).
46. Anderson, S. A. et al. The IRP1-HIF-2 α axis coordinates iron and oxygen sensing with erythropoiesis and iron absorption. *Cell Metab.* **17**, 282–290 (2013).
47. Galy, B., Ferring, D., Benesova, M., Benes, V. & Hentze, M. W. Targeted mutagenesis of the murine IRP1 and IRP2 genes reveals context-dependent RNA processing differences in vivo. *RNA* **10**, 1019–1025 (2004).
48. Ghosh, M. C. et al. Deletion of iron regulatory protein 1 causes polycythemia and pulmonary hypertension in mice through translational derepression of HIF2 α . *Cell Metab.* **17**, 271–281 (2013).
49. LaVaute, T. et al. Targeted deletion of the gene encoding iron regulatory protein-2 causes misregulation of iron metabolism and neurodegenerative disease in mice. *Nat. Genet.* **27**, 209–214 (2001).
50. Wilkinson, N. & Pantopoulos, K. IRP1 regulates erythropoiesis and systemic iron homeostasis by controlling HIF2 α mRNA translation. *Blood* **122**, 1658–1668 (2013).
51. Kristensen, A. R., Gsponer, J. & Foster, L. J. A high-throughput approach for measuring temporal changes in the interactome. *Nat. Methods* **9**, 907–909 (2012).
52. Christova, T. & Templeton, D. M. Effect of hypoxia on the binding and subcellular distribution of iron regulatory proteins. *Mol. Cell Biochem.* **301**, 21–32 (2007).
53. Patton, S. M., Piñero, D. J., Surguladze, N., Beard, J. & Connor, J. R. Subcellular localization of iron regulatory proteins to Golgi and ER membranes. *J. Cell Sci.* **118**, 4365–4373 (2005).
54. Wang, J. W., Beck, E. S. & McCabe, B. D. A modular toolset for recombination transgenesis and neurogenetic analysis of *Drosophila*. *PLoS One* **7**, e21202 (2012).
55. Gratz, S. J. et al. Highly specific and efficient CRISPR/Cas9-catalyzed homology-directed repair in *Drosophila*. *Genetics* **196**, 961–971 (2014).
56. Port, F., Chen, H. M., Lee, T. & Bullock, S. L. Optimized CRISPR/Cas tools for efficient germline and somatic genome engineering in *Drosophila*. *Proc. Natl Acad. Sci. USA* **111**, E2967–E2976 (2014).
57. Port, F. & Bullock, S. L. Augmenting CRISPR applications in *Drosophila* with tRNA-flanked sgRNAs. *Nat. Methods* **13**, 852–854 (2016).
58. Huang, D. W. et al. The DAVID Functional Classification Tool: a novel biological module-centric algorithm to functionally analyze large gene lists. *Genome Biol.* **8**, R183 (2007).
59. Prithviraj, R., Trunova, S. & Giniger, E. Ex vivo culturing of whole, developing *Drosophila* brains. *J. Vis. Exp.* **65**, 4270 (2012).
60. González, M. et al. Generation of stable *Drosophila* cell lines using multicistronic vectors. *Sci. Rep.* **1**, 75 (2011).
61. Gao, M., McCluskey, P., Loganathan, S. N. & Arkov, A. L. An in vivo crosslinking approach to isolate protein complexes from *Drosophila* embryos. *J. Vis. Exp.* doi 10.3791/51387 (2014).
62. Gerace, E. & Moazed, D. Affinity pull-down of proteins using Anti-FLAG M2 agarose beads. *Methods Enzymol.* **559**, 99–110 (2015).
63. Elias, J. E. & Gygi, S. P. Target-decoy search strategy for increased confidence in large-scale protein identifications by mass spectrometry. *Nat. Methods* **4**, 207–214 (2007).
64. Elias, J. E. & Gygi, S. P. Target-decoy search strategy for mass spectrometry-based proteomics. *Methods Mol. Biol.* **604**, 55–71 (2010).
65. Jabbour, R. E. & Snyder, A. P. In *Biological Identification* (ed Schaudies, R. P.) 370–430 (Woodhead Publishing, 2014).
66. Khan, S. J., Abidi, S. N., Tian, Y., Skinner, A. & Smith-Bolton, R. K. A rapid, gentle and scalable method for dissociation and fluorescent sorting of imaginal disc cells for mRNA sequencing. *Fly. (Austin)* **10**, 73–80 (2016).
67. Deutsch, E. W. et al. The ProteomeXchange consortium in 2017: supporting the cultural change in proteomics public data deposition. *Nucleic Acids Res* **45**, D1100–D1106 (2017).
68. Perez-Riverol, Y. et al. The PRIDE database and related tools and resources in 2019: improving support for quantification data. *Nucleic Acids Res* **47**, D442–D450 (2019).
69. Hendrickson, D. G. et al. Concordant regulation of translation and mRNA abundance for hundreds of targets of a human microRNA. *PLoS Biol.* **7**, e1000238 (2009).
70. Khalil, A. M. et al. Many human large intergenic noncoding RNAs associate with chromatin-modifying complexes and affect gene expression. *Proc. Natl Acad. Sci. USA* **106**, 11667–11672 (2009).
71. Rinn, J. L. et al. Functional demarcation of active and silent chromatin domains in human HOX loci by noncoding RNAs. *Cell* **129**, 1311–1323 (2007).
72. Kohler, S. A., Henderson, B. R. & Kühn, L. C. Succinate dehydrogenase b mRNA of *Drosophila melanogaster* has a functional iron-responsive

element in its 5'-untranslated region. *J. Biol. Chem.* **270**, 30781–30786 (1995).

73. Surdej, P., Richman, L. & Kühn, L. C. Differential translational regulation of IRE-containing mRNAs in *Drosophila melanogaster* by endogenous IRP and a constitutive human IRP1 mutant. *Insect Biochem Mol. Biol.* **38**, 891–894 (2008).

Acknowledgements

The authors thank the Bloomington *Drosophila* Stock Center at Indiana University, and the Vienna *Drosophila* Resource Center for sending fly stocks. We thank the labs of Henry Krause and Michael O'Connor for providing fly stocks, and we also thank Andrew Simmonds for sharing vectors and cell culture tools with us. We extend our thanks to Fanis Missirlis and Arash Bashirullah for insightful comments and discussions. K.K.J. wishes to thank the CIHR for supporting this work (MOP 93761). R.L. acknowledges the generous financial support from Deutsche Forschungsgemeinschaft (Koselleck grant LI 415/6), and networking support from the COST Action FeSBioNet (Contract CA15133).

Author contributions

N.H. co-designed experiments and carried out most experiments, Q.O. conducted the RNAi screen and initial phenotypic characterization, P.C. generated IRP1 transgenic lines and analyzed NOS^{IR-X} phenotypes. R.L. trained Q.O. in iron-related experiments, provided reagents and had an advisory role throughout the project. K.K.J. analyzed the RNA-Seq data, supervised and co-designed experiments, and wrote the manuscript with input from the other authors.

Competing interests

The authors declare no competing interests.

Additional information

Supplementary information is available for this paper at <https://doi.org/10.1038/s41467-019-13237-8>.

Correspondence and requests for materials should be addressed to K.K.-J.

Peer review information *Nature Communications* thanks Hasan Akman, Claudia Blindauer and the other, anonymous, reviewer(s) for their contribution to the peer review of this work. Peer reviewer reports are available.

Reprints and permission information is available at <http://www.nature.com/reprints>

Publisher's note Springer Nature remains neutral with regard to jurisdictional claims in published maps and institutional affiliations.



Open Access This article is licensed under a Creative Commons Attribution 4.0 International License, which permits use, sharing, adaptation, distribution and reproduction in any medium or format, as long as you give appropriate credit to the original author(s) and the source, provide a link to the Creative Commons license, and indicate if changes were made. The images or other third party material in this article are included in the article's Creative Commons license, unless indicated otherwise in a credit line to the material. If material is not included in the article's Creative Commons license and your intended use is not permitted by statutory regulation or exceeds the permitted use, you will need to obtain permission directly from the copyright holder. To view a copy of this license, visit <http://creativecommons.org/licenses/by/4.0/>.

© The Author(s) 2019